The Dissertation Committee for Junwei Huang
certifies that this is the approved version of the following dissertation:

Scanning Probe Microscopy Investigation of Bilayered Manganites

Committee:

Alex de Lozanne, Supervisor

John T. Markert

John T. McDevitt

Chih-Kang Shih

Zhen Yao

Scanning Probe Microscopy Investigation of Bilayered Manganites

by

Junwei Huang, B.S., M.S.

DISSERTATION
Presented to the Faculty of the Graduate School of
The University of Texas at Austin
in Partial Fulfillment
of the Requirements
for the Degree of

DOCTOR OF PHILOSOPHY

THE UNIVERSITY OF TEXAS AT AUSTIN
August 2007

to my wife, my parents and my sister.

Acknowledgments

I have many people whom I would like to thank not only for their help in completing my Ph.D. work but also for making my work and life much easier here. First, I would like to thank my advisor Dr. Alex de Lozanne. Alex has been a great person to work with. He always has many quick ideas to solve tough problems and a lot of hand-on experience to direct me to finish my instrumental work. The most important knowledge I learned from him is how to design and construct a scanning probe microscope. He also spent a lot of time in reading this dissertation and correcting spelling and grammar mistakes I made, which I really appreciate.

I would also like to thank Dr. Jinho Lee, Dr. Liuwan Zhang and Dr. Ayan Guha. Jinho taught me some tricks in machining small STM parts the first time when I worked in the student machine shope. Dr. Zhang liked to share with me his new MFM results and his understanding in physics. I would particularly like to thank Ayan for all the help he has given to me in learning about the electronics used in an STM and in building my ESR-STM. Thanks also goes to Dr. Casey Israel and Dr. Weida Wu. Casey helped me a lot in getting familiar with the Veeco Nanoscope software and in interpreting STM and AFM results. He was always the first person I asked for help when I encountered problems during running experiments. Weida is a kind and patient listener. He answered me a lot of questions about physics. I really enjoyed discussing physics or daily life with him.

Special thanks goes to my collaborator Dr. Jeehoon Kim. He made enormous efforts to reconstruct and optimize the low temperature scanning tunneling microscope (LTSTM). Without his efforts, I would not have had a LTSTM to work with. I will miss the moment when we worked together to solve instrumental problems and to figure out the physics behind the data we obtained. I would also like to thank Dr. Tien-Ming Chuang. Ming helped me conduct MFM measurement on a bilayered manganite sample, which was very important to me. He brought a lot of fun to the lab. I enjoyed talking with him about the latest news in the physics circle. I would also like to thank the other labmates, Changbae Hyun, Suenne Kim, Seongsoo Kweon, Alfred Lee, Frank Ruzicka and Morgann Berg for their help on my research and their kindness. I felt so fortunate to have such a group of great people to work with. Thanks especially goes to Changbae, who helped me finish the MFM measurement. He led me to go through almost all the Korean restaurants in Austin during the past years. I really enjoyed this hot and tasty Korean food. I would also like to say thanks to Alex Khajetoorians and Shengyong Qin in Dr. Shih's lab for sharing their experience of STM with me. I enjoyed discussing with them about technical issues in STM.

I would also like to acknowledge some of my great collaborators, Dr. John Mitchell at Argonne National Lab, Dr. Jianshi Zhou and Dr. John Goodenough in the department of mechanical engineering at UT. Dr. Mitchell

provided us high quality single crystal samples. Dr. Zhou and Dr. Goodenough developed a theoretical model to interpret our results. I learned a lot of physics in transition metal oxides from them.

The staff in the machine shop, cryogenic shop, electronics repair shop and physics storeroom have been very helpful over the years. I would like to thank them, in particular, Jack Clifford, Allan Schroeder, Ed Baez, Lanny Sandefur, Robert Hasdorff, Gary Thomas and David Elias. This work would not have been possible without their help.

Finally, I would like to thank my wife Pei, my parents and my sister for all of their love, understanding and support during my time at UT.

Scanning Probe Microscopy Investigation of Bilayered Manganites

Publication No. __________________

Junwei Huang, Ph.D.
The University of Texas at Austin, 2007

Supervisor: Alex de Lozanne

The bilayered manganite $La_{2-2x}Sr_{1+2x}Mn_2O_7$, with x in the ferromagnetic compositional region, exhibits very interesting electronic and magnetic properties below the Curie temperature, such as a colossal magneto-resistance (CMR) effect. We have studied the microscopic electronic structure in the x = 0.32, 0.4 compounds at 80 K and 20 K by using a home-built low temperature scanning tunneling microscope (STM) and the evolution of the ferromagnetic domains with temperature and magnetic field in the x = 0.32 compound from 30 K to 110 K by using a home-built low temperature magnetic force microscope (MFM).

STM topographic images show nano-sized patterns composed of Mn^{3+}-rich and Mn^{4+}-rich regions in the mixed-valent matrix. Tunneling spectra $I(V)\&\frac{dI}{dV}(V)$ show a gap and a tunneling asymmetry of the LDOS as a function of the sample bias voltage. By using current-imaging tunneling spectroscopy (CITS), we obtained a series of tunneling conductance maps which show the coexistence of localized electrons and itinerant electrons in this system. In the x = 0.32 compound, we observed a modulation with a wave vector of 16 $\AA$ propagating along a-axis at 20K. This indicates the formation of a charge density wave as a result of Fermi surface nesting in this system.

In MFM images, we observed that below 60 K, the ferromagnetic (FM) domains form stable treelike patterns and the domains are mainly oriented in the out-of-plane direction. As the temperature increases, the FM domains begin to experience a gradual change. This change becomes more and more rapid above 80 K. The FM domains change their magnetization from the out-of-plane direction to in-plane around 88 K. The in-plane FM domains completely disappear near T_C . We also observed thermal hysteresis occurring in magnetic structures. We conclude that the formation of FM domains at low temperatures is determined by the energy associated with surface magnetic free poles and domain walls. At high temperatures, the two-dimensional ferromagnetic fluctuation in the basal plane may also play an important role in forming the domain structures.

Table of Contents

List of Tables

List of Figures

Chapter 1

Introduction to Scanning Tunneling Microscopy

Since the first scanning tunneling microscope (STM) was invented by Binnig and Rohrer in 1982 [1], it has become a sophisticated surface analytical tool and been widely used in surface science to explore the microscopic electronic structures of metals [2], semiconductors [3] [4] and superconductors [5] [6], and to manipulate individual atoms or spin moments on various substrates [7] [8]. Nowadays, an STM can be commonly incorporated with a vacuum or cryogenic system for special application purposes. The whole STM system turns out to be very complicated and very costly. But the operating mechanism of an STM always remains the same. In an STM unit, a sharp conducting tip works as a probe and it is scanned with respect to a conducting sample to be studied. The tip is brought so close to the sample that a net tunneling current flows as a bias voltage is applied in between them. The tunneling current can be measured as a function of location (x,y), bias voltage V and tip-sample separation z. By operating the STM in different modes, one would be able to obtain several important quantities of the sample, such as topography, local density of states, apparent barrier height, etc. The essential parts of an STM are:

1. Tip. Usually, it is a metal tip which is clean and sharp. It is supposed to have a known and well-defined density of states near the Fermi energy.

2. Sample. The sample under study can be a metal, semiconductor, superconductor or other material such as a manganite or a ruthenate, as long as the material has enough conductivity.

3. Scanner. Scanners are made of piezoelectric materials (lead zirconate titanate ceramics (PZT)). In the early years of STM instrumentation, people used tripod piezoelectric scanners. Later, the tripod scanner was replaced by the tube scanner because the latter has higher mechanical resonance frequency and better body rigidity. We use a PZT-5H tube scanner in our low temperature scanning tunneling microscope (LT-STM). The outer wall of our tube scanner is equally divided into four quadrants. The tube scanner will extend or retract in response to the external voltage applied in between the inner and outer wall. In our LTSTM, the sample is mounted on the scanner.

4. Walker. The walker is used to bring the tip and sample into a tunneling distance. Our walker is adapted from the Attocube design, which is one type of inertia motor. It is driven by a home-built sawtooth generator called walker driver.

5. Electronics and Computer. An x,y scan board, which generates a triangle wave form, is needed to drive the tube scanner to scan along the x and y directions. A feedback board is used to keep the tunneling current

fixed at a setpoint by adjusting the voltage responsible for making the tube scanner move along z direction. A computer collects and records all the data through a data acquisition board. All the electronics are commercially available. We use a RHK SPM100 controller.

A basic STM system is illustrated schematically in figure 1.1. The specifications of our home-built low temperature scanning tunneling microscope (LTSTM) are available in appendix A.

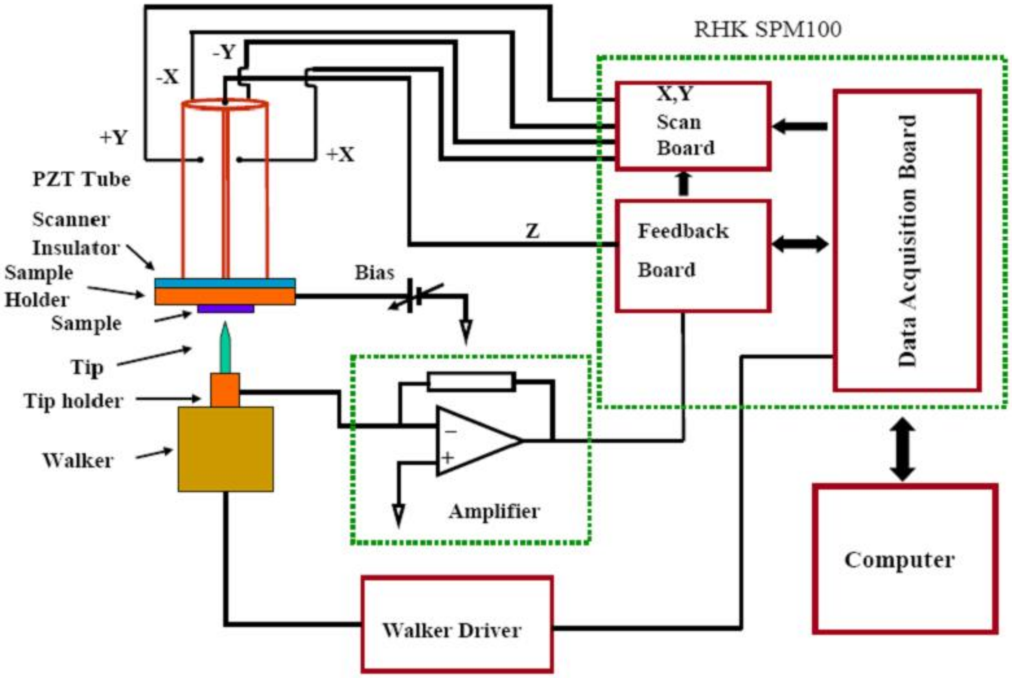

Figure 1.1: Schematic of a scanning tunneling microscope.

1.1 Theory of Scanning Tunneling Microscopy

In 1960, Bardeen developed a time-dependent perturbation approach to calculate the tunneling current through a metal-insulator-metal junction [9]. Tersoff and Hamann first successfully applied Bardeen's approach to explain topographic STM images of superstructures of Au (110) surfaces [10] [11]. In Bardeen's approach, the STM tip and sample are treated as two separated electrodes in which the electrons obey Fermi-Dirac distributions. The electrons tunnel through the vacuum barrier from one side to the other, see figure 1.2.

With a negative bias voltage V applied to the sample, the next tunneling current can be evaluated in the following way:

$$\begin{aligned} I &= I_{S\to T} - I_{T\to S} \\ &= \frac{4\pi e}{\hbar}\int_{-\infty}^{\infty}[f(E_F - eV + \epsilon) - f(E_F + \epsilon)]\rho_S(E_F - eV + \epsilon)\rho_T(E_F + \epsilon)|M|^2\,d\epsilon \end{aligned} \tag{1.1}$$

where $f(E) = \{1 + \exp[(E - E_F)/\kappa_B T]\}^{-1}$ is the Fermi distribution function; $\rho_S(E)$ and $\rho_T(E)$ are the density of states (DOS) of the sample and tip respectively; M is the tunneling matrix element [12].

Assuming that the Fermi surface of the tip and sample does not smear out much, namely, $\kappa_B T$ is much smaller than the energy resolution required in the experiment, one can approximately treat the Fermi distribution function as a step function. Then the tunneling current can be simplified as:

$$I \approx \frac{4\pi e}{\hbar}\int_{0}^{eV} \rho_S(E_F - eV + \epsilon)\rho_T(E_F + \epsilon)|M|^2\,d\epsilon \tag{1.2}$$

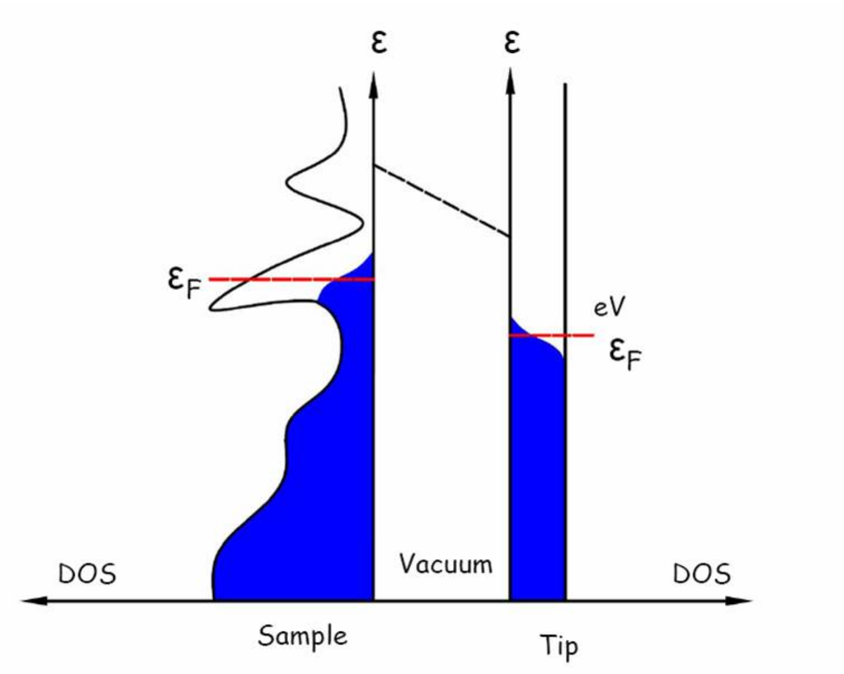

Figure 1.2: Schematic of a tunneling process. The sample with unknown DOS is on the left and the tip with almost constant DOS is on the right. The sample is biased with a negative voltage V with respect to the tip. Net electrons tunnel from the sample to tip through the vacuum barrier. The vertical direction is energy and the horizontal direction is DOS.

The tunneling matrix element M changes very slowly within the energy interval eV and can be treated as a constant in the integrand of Eqn. 1.2. Therefore it is evident from Eqn. 1.2 that the convolution of the DOS of the tip and sample is responsible for the total tunneling current. The tip is usually made of metal wires such as tungsten or platinum, which have an almost constant DOS near E_F. Taking the first order derivative on both sides of Eqn. 1.2 with respect to V, one finds the tunneling conductance:

$$\frac{dI}{dV}(V) \propto \rho_S(E_F - eV) \tag{1.3}$$

Which means the tunneling conductance is proportional to the DOS of the sample at $E_F - eV$! Therefore we can map out the spatial distribution of the DOS of a sample at the nanoscale, enabling us to understand most electronic properties of the sample. The STM is exactly suitable to do this kind of work.

The tunneling matrix M in Eqn. 1.2 plays a very important role in determining the vertical and lateral resolution of the STM. It can be expressed as:

$$M = -\frac{\hbar^2}{2m}\int_{\Sigma}(\Phi^*\nabla\Psi - \Psi\nabla\Phi^*) \cdot d\mathbf{S} \tag{1.4}$$

where Φ is the wavefunction of the tip and Ψ is the wavefunction of the sample; the surface integral is evaluated within the tunneling barrier. If the tilt of the vacuum barrier caused by the applied bias voltage is negligibly small compared to the work function of the tip and sample, which is true in most cases, $|M|^2$ is approximately equal to the probability of the electron tunneling from the sample to tip through a square barrier, see figure 1.2.

$$|M|^2 \propto exp(-2\kappa Z) \tag{1.5}$$

where $\kappa = \frac{\sqrt{2m\phi}}{\hbar}$ is called the decay constant. Usually, the decay constant is about one $\mathring{A}^{-1}$ for metals. For example, the work function of platinum is $\phi = 5.7eV$, which results in $\kappa = 1.21\mathring{A}^{-1}$. By substituting Eqn. 1.5 into Eqn. 1.2, one obtains:

$$I \propto \rho_S(E_F)exp(-2\kappa Z)\int_0^{eV} \rho_T(E_F - eV + \epsilon)\, d\epsilon \tag{1.6}$$

the tunneling current changes exponentially with the tip-sample separation Z. The exponential dependence of tunneling current on Z enables the STM to reach subatomic vertical resolution. On the other hand, the tunneling current depends on the electron density of the sample near E_F within the energy interval of eV (the integral term). For metals, the electron density near E_F is quite high, so only a small bias voltage is applied, typically several tens of mV to obtain several nA in tunneling current. But for semiconductors or some poor metals such as manganites and ruthenates, a bias voltage as high as 1V is applied to obtain a hundred pA tunneling current; the tunneling matrix element no longer takes the simple form shown in Eqn. 1.5, and therefore the tilt of the vacuum barrier should be seriously taken into account to calculate the tunneling matrix element.

1.2 STM Operation Modes

An STM can work in different modes according to what type of data are needed to be collected. Basically, there are three types of operation modes: topography mode, single-point tunneling spectroscopy (SPTS) mode and constant-imaging tunneling spectroscopy (CITS) mode. People may use different names for these modes. I will describe those modes in detail in this section.

1.2.1 Topography

In the topography mode, the tip rasters over the sample and traces out the height contour of the sample surface. To do so, the feedback loop is used to keep the tunneling current constant, which means the tip-sample separation is kept constant, and the voltages making the scanner move along the z direction are simultaneously recorded and converted into height data. Because the STM probes the DOS within the energy interval eV near E_F, the electronic height measured by the STM may be different from the physical height of the sample in the case that the sample is a mixture of different materials or it is electronically inhomogeneous.

As an example, figure 1.3 shows topographic images of layered $\mathrm{Sr_2RuO_4}$ and highly ordered pyrolytic graphite (HOPG) obtained by our LTSTM at 80 K. Figure 1.3 (a) shows 800 nm × 800 nm scan size flat surface of cleaved $\mathrm{Sr_2RuO_4}$, where several steps are visible. Individual graphite atoms are resolved in figure 1.3 (b) (scan size 1.5 nm × 1.5 nm). A line profile along the blue line in figure 1.3 (b) shows the atomic corrugation.

1.2.2 Single-Point Tunneling Spectroscopy (SPTS)

As mentioned in Eqn. 1.3, the tunneling conductance $\frac{dI}{dV}(V,x,y)$ is proportional to the DOS of the sample. It is a function of bias voltage and position. In the SPTS mode, the tip is parked at a position of interest for about a minute until it gets stable. Then the feedback is turned off so that the tip-sample separation is fixed. The bias voltage is ramped up and down

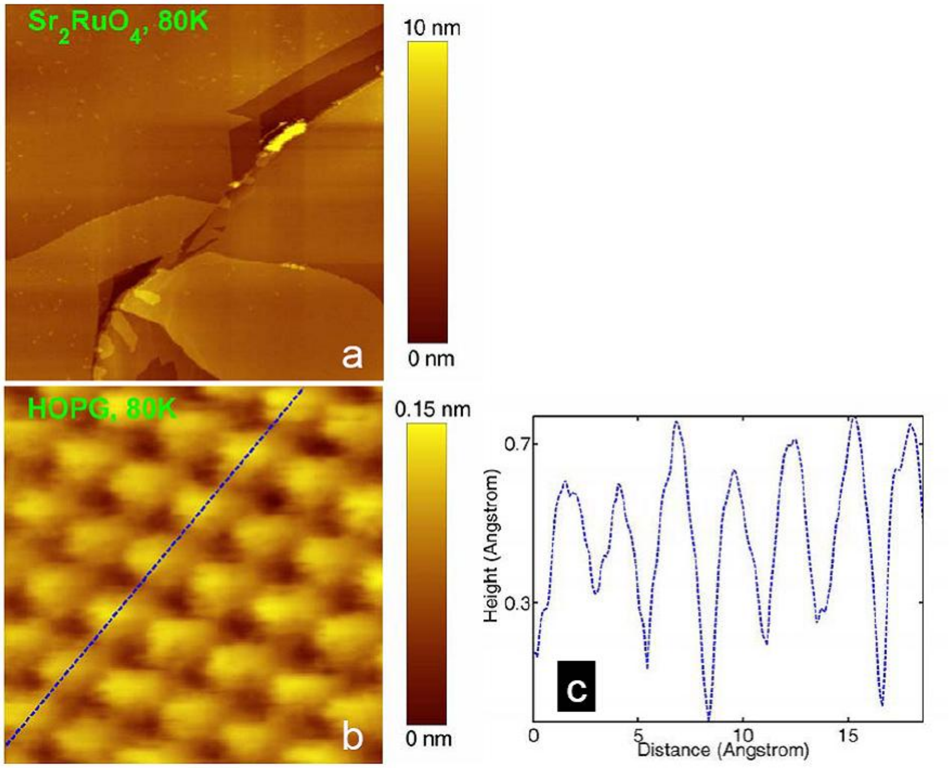

Figure 1.3: (a) topography of Sr$_2$RuO$_4$, I$_T$ = 100 pA, V$_{Bias}$ = -200 mV. (b) tpography of HOPG, I$_T$ = 180 pA, V$_{Bias}$ = 350 mV. (c) line profile along the blue line in (b).

and the corresponding tunneling current is recorded. So one can plot I(V) curves at a certain position. By numerically taking $\frac{dI}{dV}$, we can have the tunneling conductance vs. voltage at that position. Another way to obtain a $\frac{dI}{dV}(V)$ curve is by using the lock-in technique. When a small sinusoidal voltage with a frequency ω is added to the ramping bias voltage, the amplitude of the first harmonic of the tunneling current is proportional to the tunneling conductance. This can be easily seen by expanding the tunneling current into a Taylor series:

$$I(V + \Delta V sin\omega t) \approx I(V) + \frac{dI}{dV}\Delta V sin\omega t + O((\Delta V)^2) \qquad (1.7)$$

Lock-in amplifiers are widely used to directly obtain the tunneling conductance by STM research groups around the world. We used both methods to take the tunneling conductance (see appendix C for the lock-in technique.).

1.2.3 Current-Imaging Tunneling Spectroscopy (CITS)

In the SPTS mode, one is able to obtain the tunneling conductance at one point in a topographic image. It would be nicer to know the complete tunneling conductance at each point in a topographic image with a fixed tip-sample separation. Hamers *et al.* first proposed this method and applied it to image Si(1,1,1)-7×7 [13]. In the CITS mode, I(V) or $\frac{dI}{dV}$ curves at each point in a topography are simultaneously obtained with the topography. At each point, the feedback is first turned on to take the topography and then turned off to take I(V) or $\frac{dI}{dV}$ curves. From a set of CITS data, one can extract tunneling conductance maps at different bias voltages, namely, one can obtain the real-space DOS distribution of the sample at different energy with respect to E_F. By performing a fast Fourier transform (FFT) on the tunneling conductance maps, one can numerically calculate the K space DOS distribution, with which many electronic properties of the sample can be explained.

1.3 Tip Preparation

We mainly use platinum and iridium (Pt/Ir) alloy tips. We make the tips out of 0.01" Pt/Ir wires by electrochemically etching them in a calcium chloride aqueous solution; see appendix B for details. It is hard to make a very sharp Pt/Ir tip because Pt and Ir have different etching rates in etchant and both metals are very resistant to chemicals. We etch the tips in two steps [14]. In the first step, the tip is roughly etched at a high AC voltage (~ 35 V); in the second step, a small AC voltage (~ 2 V) is used and the tip is reshaped and cleaned by finely etching its very end. Before being loaded in the STM chamber, every tip is carefully rinsed in distilled water in order to remove the impurities attached on the end of the tip. In the STM chamber, the tips are *in situ* cleaned by electron beam heating. Possible water molecules or oxides at end of the tip should be removed by electron beam heating.

We also tried tungsten tips. But the W tips did not give us consistent results. So we stick to Pt/Ir tips. As a matter of fact, many STM groups around the world prefer to use tungsten tips because they are cheap and can be made very sharp. One problem about the tungsten tip is that it is very easy to be oxidized. The thick oxide at the apex of the tip must be removed *in situ.*

1.4 Sample Preparation

Most of the samples we are interested in are single-crystal transition metal oxides(TMOs), such as $YBa_2Cu_3O_{7-\delta}$, $La_{2-2x}Sr_{1+2x}Mn_2O_7$ and Sr_2RuO_4.

In order to keep the exposed sample surface free of contamination, we need to *in situ* cleave the sample in the ultra-high vacuum(UHV) STM chamber. As a common sense, the smaller a sample is, the more easily it can be cleaved. This is even true for layered single-crystal samples. Furthermore, most of the single-crystal TMOs are grown in very small sizes ($\sim mm^3$) due to technical difficulties. So the STM samples we prepare are usually very small, typically 0.03” in diameter. We use electrically conductive silver epoxy to glue the sample on the protrusion portion (∼ 0.03” in Dia.) of a sample holder, which is made of oxygen free high conductivity copper, and then put a short copper wire, with ∼ 0.03” in diameter, on the top surface of the sample bonded by general purpose epoxy. We file off the excess part of the sample and glue until it is flush with the copper and the sample holder, see figure 1.4. The prepared sample will be cleaved in the STM chamber by hitting the copper wire against the edge of the cold finger shielding window.

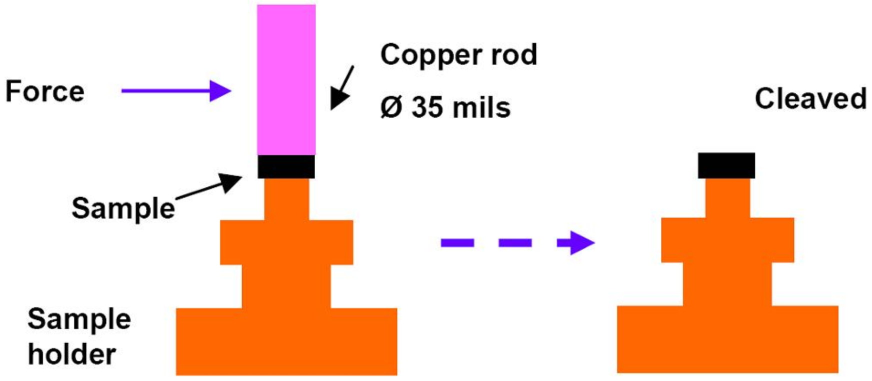

Figure 1.4: Schematic of sample cleaving procedure.

1.5 Performance of our STM

Our LTSTM is located on the 13th floor of the RLM building. We used a Bruel Kjar 8318 accelerometer to measure the vibrational noise on the LTSTM chamber. The noise spectrum shows a large peak at 18 Hz along with other small peaks. We attribute the peak at 18 Hz to the intrinsic building vibrational noise. To attenuate this vibrational noise, we mounted our LTSTM chamber on three newport isolators(two XL-A, one XL-B). These isolators effectively reduce low frequency vibrational noise, which can be seen from the noise spectrum shown in figure 1.5. The two main sources of noise that limit the scan resolution of our LTSTM are electrical noise arising from the tunneling current amplifier and the vibrational noise caused by liquid nitrogen bubbling in the outer dewar and inner dewar when filled with LN2. We should be able to reduce the noise level by choosing a better current amplifier and designing a more effective damping system for the STM head. But our STM still can achieve 0.1 $\AA$ z resolution and about 2 $\AA$ lateral resolution.

The STM can stably work at room temperature, 80 K and 20 K. Most of the time it is operated at 80 K and 20 K. The STM head can reach 80K when both inner and outer dewar of the STM are filled with LN_2. When the inner dewar is filled with LHe_2 and the outer dewar is filled with LN_2, the STM head can be cooled down to 20 K. The reason why the STM head can not reach the temperature of the cooling liquids is that the cooling power transfered to the STM head is not enough because the STM head is suspended by steel springs from the cold finger and the cold shielding is very long. When

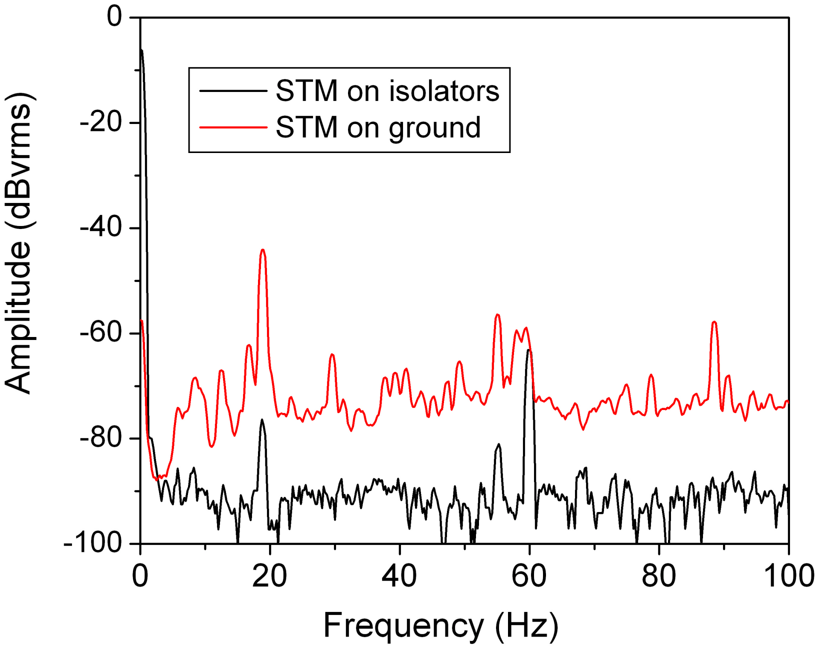

Figure 1.5: Vibrational noise spectra taken on the STM.

the STM head is locked against two lobes attached on the cold shielding, it can reach 79 K with LN_2 cooling and 16 K with LHe_2 cooling. More details about our LTSTM are available in Dr. Jeehoon Kim's Ph.D. Dissertation, 2007. A concise specification of the STM can be seen in the appendix A.

Chapter 2

Properties of Manganese Perovskites

The perovskite-type manganites $R_{1-x}A_xMnO_3$, where R is a trivalent rare earth ion, A is divalent alkaline earth ion and the Mn ion is in the mixed-valent state composed of Mn^{3+} and Mn^{4+}, have been extensively studied for more than half a century. In 1994, Jin et al. [15] first observed that the resistance in $La_{\frac{2}{3}}Ca_{\frac{1}{3}}MnO_3$ thin films decreases dramatically at 77K upon applying an external magnetic field, which is known as colossal magneto-resistance (CMR) effect. Since then, great efforts have been made to understand the complexity of these materials and to increase the CMR transition temperatures so as to apply them to magnetic storage devices. The complexity of manganites originates from the delicate balance among various degrees of freedom, such as charge, orbital, spin and lattice vibrations. This balance naturally leads to multiple possible electronic and magnetic ground states that compete with each other at similar energy scales. Which state dominates in this competition is highly related to the chemical composition, charge carrier concentration, crystal structure and external parameters such as temperature, pressure and magnetic field. There are some general properties of $R_{1-x}A_xMnO_3$ perovskites that I should review. These properties can be referred to explain the magnetic ordering and electronic inhomogeneity of the bilayered LSMO that

I have studied.

2.1 Tolerance Factor

The tolerance factor of $R_{1-x}A_xMnO_3$ perovskites is defined as [16]:

$$t = \frac{(R,A) - O}{\sqrt{2}(Mn - O)} \tag{2.1}$$

Where (R,A)-O and Mn-O are equilibrium bond lengths calculated at room temperature and atmospheric pressure based on available X-ray data. The tolerance factor indicates lattice mismatch, which can be accommodated by lattice distortion occurring in crystals. For t<1, as in the case of $La_{1-x}Sr_xMnO_3$ and $La_{1-x}Ca_xMnO_3$, the crystal structure is under compression. The compressive stress can be alleviated by cooperative rotation of the MO_6 octohedra. The cooperative displacement of O^{2-} results in buckling of the average Mn-O-Mn bonding, which directly affects the ferromagnetic transition temperatures [17], see figure 2.1. For t>1, the cystal structure forms hexagonal polytypes [16] in order to minimize the elastic energy. t depends on both pressure and temperature because the thermal expansion and compressibilities of the (R,A)-O and Mn-O bonds are different. By calculating the tolerance factor, we would be able to predict the crystal structure of manganites, and then further predict the magnetic and electronic properties of the manganites according to their crystal structures.

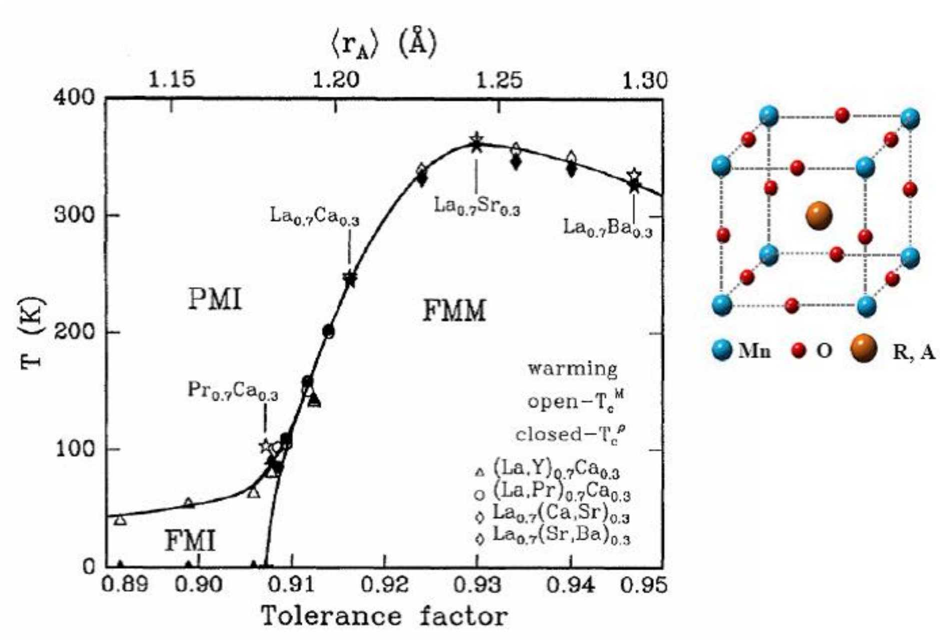

Figure 2.1: Tolerance factor vs. phase diagram of temperature for the system $R_{1-x}A_xMnO_3$. Open symbols denote T_C^M taken at 100 Oe (T_C^M is defined as a minimum in $d(M/H)/dT$); closed symbols denote T_C^ρ taken in a warming up run (T_C^ρ is defined as a minimum in $d(\log \rho)/dT$) [17]

2.2 Crystal Field Splitting

The 3d electrons in Mn play a crucial role in perovskite manganites in determining their electrical transport, magnetic ordering and lattice distortion, etc. Under a cubic field symmetry, five-fold degenerate 3d orbitals are split into triple degenerate t_{2g} (d_{xy}, d_{yz}, d_{zx}) and double degenerate e_g ($d_{x^2-y^2}$, $d_{3z^2-r^2}$). The t_{2g} and e_g orbitals will be further split under a tetragonal or rhombohedral field symmetry, see figure 2.2.

In the point-charge ionic model, the empty 3d orbitals are ΔE_p above

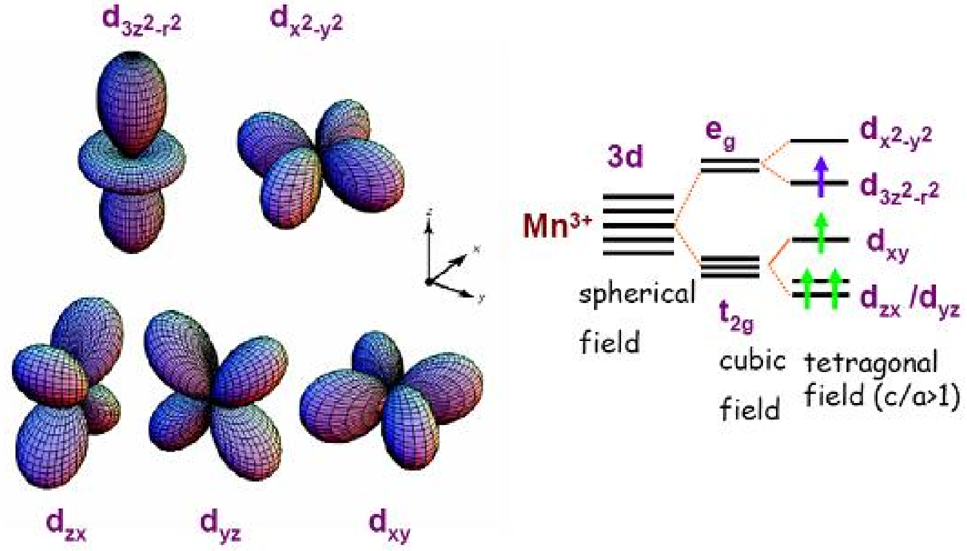

Figure 2.2: Schematic of 3d electron orbitals and orbital splitting under different crystal fields [18].

the O-2p orbitals and ΔE_s above the O-2s orbitals. The anti-bonding d-like states can be described as [16]:

$$\Phi_t = N_\pi(f_t - \lambda_\pi \phi_\pi) \tag{2.2}$$

$$\Phi_e = N_\sigma(f_e - \lambda_\sigma \phi_\sigma - \lambda_s \phi_s) \tag{2.3}$$

where the covalent-mixing parameters λ_π and λ_s satisfy $\lambda_\pi < \lambda_s \ll 1$, which indicates that the percentage of O-2p and O-2s orbitals mixing into d-like ligand-field wavefunctions Φ_π and Φ_σ is very small. According to second-order perturbation theory, the cubic-field splitting between t_{2g} and e_g is:

$$\Delta_c = \Delta_M + (\lambda_\sigma^2 - \lambda_\pi^2)\Delta E_p + \lambda_s^2 \Delta E_s \tag{2.4}$$

where Δ_M is purely electrostatic energy. The cubic-field splitting Δ_c is the same order of magnitude as the intraatomic exchange energy Δ_{ex} which forces the electron spins in atoms to be ferromagnetically coupled. For example, in $R_{1-x}A_xMnO_3$, $\Delta_c < \Delta_{ex}$, so Mn takes the high spin (HS) state (S=2 for Mn^{3+} and S=3/2 for Mn^{4+}); in $LaCoO_3$ at low temperatures,$\Delta_c > \Delta_{ex}$, so Co takes the low spin (LS) state (S=0 for Co^{3+}).

2.3 Double Exchange (DE)

The double exchange (DE) model is based on kinetic exchange that involves real electron transfer, in contrast with the direct exchange and superexchange processes which are a potential exchange not involving real electron transfer. The double exchange model was first proposed by Zener [19] and then further developed by Anderson and Hasegawa [20]. In the mixed-valent manganites, the conduction mechanism can be explained in terms of the double exchange interaction, which states that fast e_g electron transfer occurs across the Mn^{4+}-O^{2+}-Mn^{3+} bridge, namely, one electron transfers from O^{2-} to Mn^{4+} and another electron simultaneously transfers from Mn^{3+} to O^{2-}. Figure 2.3 explains the DE process.

The spin-independent resonance integrals describing electron transfer between Mn ions at position R_i and R_j across the Mn-O-Mn bridge are [16]:

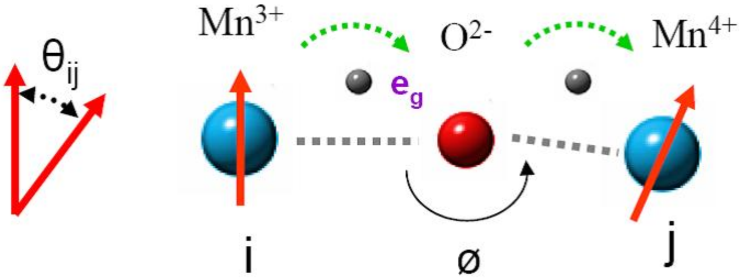

Figure 2.3: Double exchange model. ϕ is a bending angle across a Mn^{3+}-O^{2-}-Mn^{4+} bridge, which is related to the tolerance factor. θ_{ij} is the angle between the spin orientation at neighboring Mn ions. The local spins on Mn^{3+} and Mn^{4+} are not aligned as temperature is greater than the Curie temperature, but tend to be aligned parallel below T$_C$.

$$E_\pi^{cac} \equiv (\Phi_{ti}, H'\Phi_{tj}) \approx \epsilon_\pi \lambda_\pi^2. \tag{2.5}$$

$$E_\sigma^{cac} \equiv (\Phi_{ei}, H'\Phi_{ej}) \approx \epsilon_\sigma \lambda_\sigma^2 \cos\phi. \tag{2.6}$$

where the superscript cac denotes cation-anion-cation; the subscripts σ and π denote σ-bonding and π-bonding respectively; the subscripts t and e denote t$_{2g}$ and e$_g$ orbitals respectively; ϕ is a bending angle along the Mn-O-Mn bridge, see figure 2.3. H' describes the perturbation of the potential at R_i due to the presence of a Mn ion at R_j. In the absence of localized spins on the Mn ions, the tight-binding bandwidth of the π-bonding t$_{2g}$ state is:

$$W_\pi \propto \epsilon_\pi \lambda_\pi^2 \tag{2.7}$$

and of the σ-bonding e$_g$ state is:

$$W_\sigma \propto \epsilon_\sigma \lambda_\sigma^2 \cos\phi \tag{2.8}$$

The bandwidth W is a measure of the strength of the interatomic interactions, whereas the effective on-site coulomb energy U_{eff} is a measure of the strength of the intraatomic interactions. Whether the electrons are localized or itinerant depends on the competition between W and U_{eff}. The transition from localized to itinerant electronic behavior occurs where:

$$W \approx U_{eff} \tag{2.9}$$

In the CMR-manganites, W_π is generally smaller than U^π_{eff}, which leads to the localization of the t$_{2g}$ electrons; the interatomic exchange interaction for the t$_{2g}$ electrons are dominated by the antiferromagnetic superexchange interaction; while e_g electrons are at the crossover from localized to itinerant electronic behavior because W_σ competes with U^σ_{eff}. According to the double exchange model, see figure 2.3, the spin-dependent σ^* bandwidth can be expressed as:

$$W_\sigma \propto \epsilon_\sigma \lambda_\sigma^2 \cos\phi \langle \cos(\theta_{ij}/2) \rangle \tag{2.10}$$

where θ_{ij} is the angle between neighboring Mn spins. As the localized spins on the Mn ions align below a ferromagnetic transition temperature, W_σ becomes greater than U$^\sigma_{eff}$, which transforms e$_g$ electrons bound to Mn^{3+} ions into itinerant electrons occupying an antibonding σ^* band.

2.4 Virial Theorem

For the electrons in a central-force field, the virial theorem states:

$$2\langle T\rangle + \langle V\rangle = 0 \tag{2.11}$$

where $\langle T\rangle$ is the mean kinetic energy of the electrons and $\langle V\rangle$ is the mean potential energy of the electrons. The mean kinetic energy $\langle T\rangle$ of the electrons decreases discontinuously as the system changes from localized to itinerant electronic behavior. According to Eqn. 2.11, the absolute value of the mean potential energy $\langle V\rangle$ will decrease discontinuously as well [16]. A decrease in $|\langle V\rangle|$ is achieved by a decrease in Mn-O bond length because the electrons are in the antibonding state and the Mn-O bond length follows:

$$(Mn - O)_{localized} > (Mn - O)_{itinerant} \tag{2.12}$$

So this is a first-order transition. If the first-order transition occurs globally, the system will undergo a simple expansion of the lattice space without any change in its crystal symmetry. In a mixed-valent manganite, the first-order transition can occur locally because the structure allows for metal-insulator phase segregation by short-range cooperative oxygen displacements.

Chapter 3

Properties of the Bilayered Manganite $\mathbf{La_{2-2x}Sr_{1+2x}Mn_2O_7}$

In 1996, Moritomo et al. [21] successfully synthesized layered manganites having the Ruddlesden-Popper (R-P) structure. The R-P manganites have the form $La_{n+1}Mn_nO_{3n+1}$, which can be modified from the perovskite-type $LaMnO_3$ by inserting a rock-salt type block layer La_2O_2 every n MnO_2 sheets. With hole doping concentration controlled by substituting La^{3+} with Sr^{2+}, one can prepare $La_{1-x}Sr_{1+x}MnO_4$(n = 1), $La_{2-2x}Sr_{1+2x}Mn_2O_7$(n = 2),..., and up to $La_{1-x}Sr_xMnO_3$(n = ∞). Among these R-P manganites with different numbers of inserted rock-salt layers, $La_{2-2x}Sr_{1+2x}Mn_2O_7$(n=2) attracts most attention due to its very rich magnetic phases and enhanced CMR effect.

In the $La_{2-2x}Sr_{1+2x}MnO_7$, also called bilayered LSMO (see figure 3.1), neighboring bilayered (La,Sr)MnO_3 along the c-axis are misaligned due to the insertion of one (La,Sr)O block layer. So the in-plane properties of the bilayered LSMO may be similar to those of the infinite layer compound $La_{1-x}Sr_xMnO_3$ while the out-of-plane properties are close to those of rock salt type material but more conductive. Bilayered LSMO therefore shows very strong anisotropy in electrical transport and magnetization.

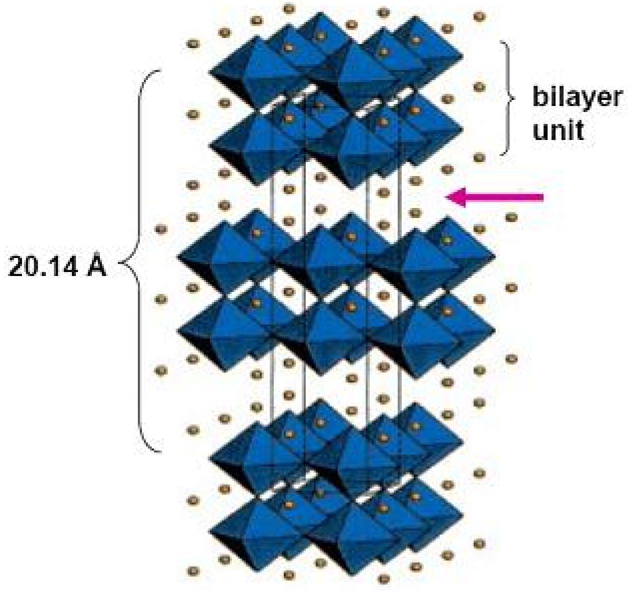

Figure 3.1: Crystal structure of a bilayered manganite [22]. The crystal has a tetragonal symmetry with $a = 3.78\mathring{A}$, $c = 20.14\mathring{A}$ [21]. The pink arrow indicates a cleavable plane.

Figure 3.2 shows the structural, electronic and magnetic phase diagram of $La_{2-2x}Sr_{1+2x}Mn_2O_7$.

3.1 Crystal Distortion

The $La_{2-2x}Sr_{1+2x}MnO_7$ has a tetragonal structure in a wide temperature range. The lattice parameters are listed in table 3.1 and table 3.2, which are adapted from [23].

In these two tables, θ denotes the out-of-plane angle between Mn and

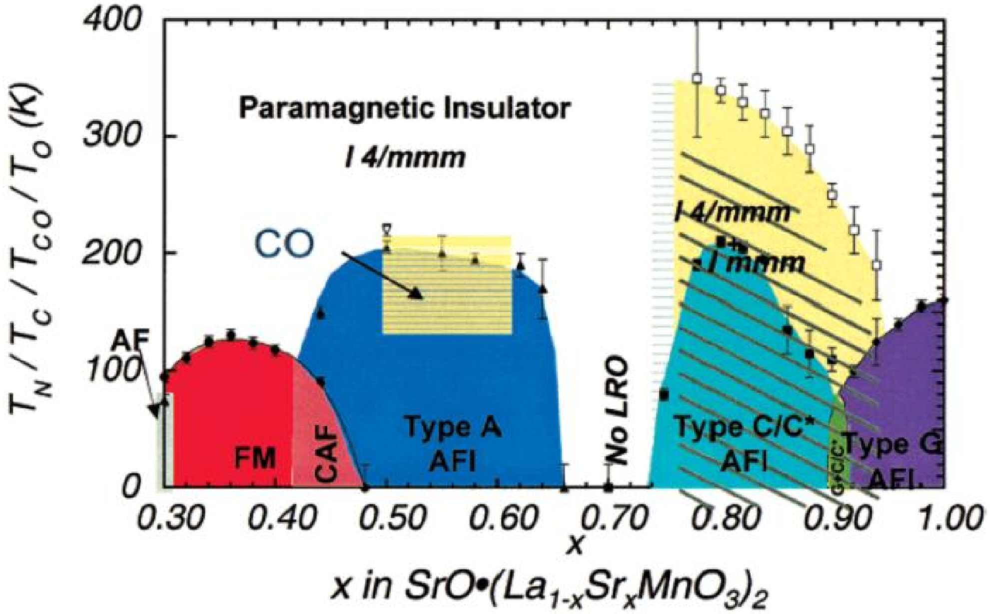

Figure 3.2: Structural and magnetic phase diagram of the bilayer manganite $La_{2-2x}Sr_{1+2x}Mn_2O_7$ [22]. FM: ferromagnetic metal; CAF: canted antiferromagnet; AFI: A-, C-, and G-type antiferromagnetic insulators. The region marked No LRO has no magnetic diffraction peaks at $T > 5K$, for more details see Ref. [22]

O(3), see figure 3.1. As can be seen from the tables, the lattice parameter a increases slightly at high and low temperature as the doping level x increases, whereas c decreases rapidly with increasing x. The variation of the lattice parameters as the doping level is closely associated with $d_{x^2-y^2}$ and $d_{3z^2-r^2}$ orbital occupancy. Both $d_{x^2-y^2}$ and $d_{3z^2-r^2}$ are antibonding orbitals. Therefore, if the $d_{x^2-y^2}$ orbital is occupied, the Mn-O equatorial bond will be elongated; if the $d_{3z^2-r^2}$ orbital is occupied, the Mn-O apical bond length will become longer. The lattice parameter variation reflects that the e_g electrons prefer to

hole concentration(x)	0.3	0.4	0.45	0.50
a(Å)	3.8600(1)	3.8711(1)	3.8729(2)	3.8748(3)
c(Å)	20.324(1)	20.126(1)	20.056(1)	20.032(1)
θ	177.7(4)	178.0(4)	177.1(3)	175.3(4)
$\langle Mn - O_{apical} \rangle$	2.012(9)	1.977(8)	1.961(8)	1.953(10)
$\langle Mn - O_{equatorial} \rangle$	1.9302(5)	1.9357(5)	1.9369(8)	1.9387(16)
Δ_{JT}	1.042(5)	1.021(4)	1.012(4)	1.007(6)

Table 3.1: Structural parameters for $La_{2-2x}Sr_{1+2x}Mn_2O_7$ at room temperature.

hole concentration(x)	0.3	0.4	0.45	0.50
a(Å)	3.8556(4)	3.8645(1)	3.8713(2)	3.8731(3)
c(Å)	20.239(2)	20.065(1)	19.952(1)	19.918(2)
θ	177.9(5)	178.9(3)	177.7(3)	177.0(4)
$\langle Mn - O_{apical} \rangle$	1.993(10)	1.972(8)	1.950(8)	1.956(9)
$\langle Mn - O_{equatorial} \rangle$	1.9280(8)	1.9323(1)	1.9360(8)	1.9370(1)
Δ_{JT}	1.034(5)	1.020(4)	1.007(4)	1.010(5)

Table 3.2: Structural parameters for $La_{2-2x}Sr_{1+2x}Mn_2O_7$ at 10K.

occupy the $d_{3z^2-r^2}$ orbital at low doping levels and the $d_{x^2-y^2}$ orbital at high doping levels. We also can see from the tables that the thermal expansion of $(Mn - O)_{apical}$ is smaller than that of $(Mn - O)_{equatorial}$. This means that upon cooling through the ferromagnetic (FM) Curie temperature (T_C = 100 K-130 K for $0.3 < x < 0.5$), the e_g electrons have the tendency to occupy the $d_{x^2-y^2}$ orbital, signaling a charge transfer from the apical to the equatorial Mn-O bond. Since different Mn-O bonds have different compressibility, external pressure will change the tolerance factor and further affect the electronic and magnetic properties. The application of hydrostatic pressure on the crystal induces magnetic phase segregation [24] and influences the competition between the t^3-O-t^3 π bonding and e^1-O-e^1 σ bonding [25]. Furthermore, a discontinuous decrease in the Mn-O bond length in these compounds was observed upon cooling through T_C [26] [27], which indicates that a first-order transition from localized to itinerant electronic behavior occurs, see Eqn. 2.11.

Jahn-Teller (JT) distortion is also responsible for the change in the lattice parameters. JT distortion factor is defined as:

$$\Delta_{JT} = \frac{\overline{(Mn-O)}_{apical}}{\overline{(Mn-O)}_{equatorial}} \tag{3.1}$$

JT distortion lifts the e_g orbital degeneracy. The fact that the Δ_{JT} is greater than 1 at at a wide temperature range indicates that it is energetically favorable for the e_g electrons to occupy the $d_{3z^2-r^2}$ orbital. In the FM metallic state, JT is suppressed by the double exchange (DE) interaction. Δ_{JT} decreases toward 1.

The striction measurement done by Kimura et al. [26] on these compounds showed that the JT distortion factor exhibits an anomaly at T_C. Upon cooling through T_C, for $x < 0.36$, Δ_{JT} decreases towards 1; for $x > 0.36$, Δ_{JT} increases; for $x = 0.36$, Δ_{JT} remains the same. The $x = 0.36$ compound, showing the highest T_C, sits at the crossover between positive and negative lattice response near T_C. This is also associated with the occupancy of the $d_{x^2-y^2}$ and $d_{3z^2-r^2}$ orbitals.

3.2 Electronic States

Compared to the infinite layer $La_{1-x}Sr_xMnO_3$ perovskite, the bilayered $La_{2-2x}Sr_{1+2x}Mn_2O_7$ exhibits an enhanced CMR effect but a lower first-order ferromagnetic transition temperature (T_C) in the FM compositional region $0.30 < x < 0.50$. When $T > T_C$, the compounds stay in a paramagnetic insulating state and their electrical transport can be described as small polaron conduction. Because the holes have the hopping time τ_h longer than the period of optical-mode lattice vibration ω_R^{-1}, they are trapped to form small polarons or Zener Mn^{3+}-O-Mn^{4+} pairs [28]. When $T < T_C$, fast hole transfer from Mn^{4+} to Mn^{3+} occurs via a strong DE because $\tau_h < \Omega_R^{-1}$. Band theory can be applied to describe the FM metallic state. Eqn. 2.3 gives the tight-binding bandwidth.

A critical question needed to be answered in all CMR-manganites is the nature of the metallic state at low temperature. Debates still exist on whether it is considered as a diffusive polaron conduction process with zero motional enthalpy or an electron scattering process with a defined Fermi surface. Experimental evidence for both scenarios has been found in the case of $La_{2-2x}Sr_{1+2x}Mn_2O_7$. Transport measurements done by Zhou et al. [28] on the $x = 0.4$ compound support the diffusive polaron conduction model. Zhou el al. measured the thermoelectric power along the c-axis and in the ab plane under hydrostatic pressure and concluded that the transport mechanism in the ab plane can be described as Mn^{3+}-O-Mn^{4+} Zener pair diffusion with a small motional enthalpy, whereas the transport mechanism along c-axis can be considered as conventional small polaron diffusion. As the temperature goes down, mobile Zener polarons confined in the ab plane are progressively trapped, and then released on further cooling to form polaron clusters near T_C. The condensation of correlated polarons driven by strong polaron-polaron interactions below T_C gives rise to a global FM phase. Transport along the c-axis requires electron transfer through a Mn-O-O-Mn bridge. This transfer process requires the donor e orbital in Mn^{3+} to be oriented along c-axis and the receptor Zener pair to have an empty e orbital oriented along the same direction. Therefore the transport along c-axis is very sensitive to the stabilities of the $d_{x^2-y^2}$ and $d_{3z^2-r^2}$ orbitals.

Angle-resolved photoemission spectroscopy (ARPES) investigations on the $x = 0.4$ compound [29] revealed the existence of a quasiparticle peak along (0,0) to ($\pm\pi$,$\pm\pi$) direction (nodal direction) and strong suppression of the spectral weight along (0,0) to ($\pm\pi$,0) and (0,$\pm\pi$) direction (antinodal direction) near the Fermi level (E_F). Suppression of the spectral weight near E_F gives rise to a pseudogap. Much as in high temperature superconductors, the Fermi surface maps show well-nested straight sections along the antinodal direction. The nested Fermi surface indicates possible formation of charge density waves (CDWs). Indeed, we observed a CDW with a long wave length in the conduction maps for the $x = 0.32$ compound with our low temperature scanning tunneling microscope (LTSTM), see chapter 4. Our STM data of the $x = 0.32$ and 0.40 compounds show hole-rich Mn^{4+} clusters and hole-poor Mn^{3+} clusters are randomly distributed at low temperatures, which signals the compounds may be considered as a polaronic metal even at low temperatures.

3.3 Magnetic Ordering

The $La_{2-2x}Sr_{1+2x}Mn_2O_7$ is a quasi-two-dimensional manganite. The inter-bilayer magnetic coupling (J_{cc}) along the c-axis is relatively weak. The doped hole concentration can dramatically influence J_{cc}. As x changes from 0.30 to 0.50, the inter-bilayer magnetic coupling evolves from antiferromagnetic (AF) to ferromagnetic (FM) and back to antiferromagnetic, which was revealed by neutron diffraction [30] [31], see figure 3.3. The interlayer magnetic coupling (J_{ac}) in a bilayer unit is slightly stronger than J_{cc}. The intra-layer magnetic coupling (J_{aa}) in the basal plane is the strongest and it remains FM in the range $0.30 < x < 0.50$. In the FM ground state, the magnetization is oriented along the c-axis with low hole concentration ($x < 0.33$), but switches to the ab plane as x becomes larger than 0.33. The change in magnetization orientation by 90^0 takes place within a small doping range from 0.32 to 0.33. The change in magnetic states with the doping level is a result of the strong magnetic competition between AF superexchange and FM double exchange and can be explained in terms of Goodenough's rules for Mn-O-Mn magnetic exchange interaction [32].

Among the important competing terms in the magnetic energy determining the magnetic ordering states are crystal field and dipole-dipole interaction. In a tetragonal system, the magnetic anisotropy energy can be expressed as [33]:

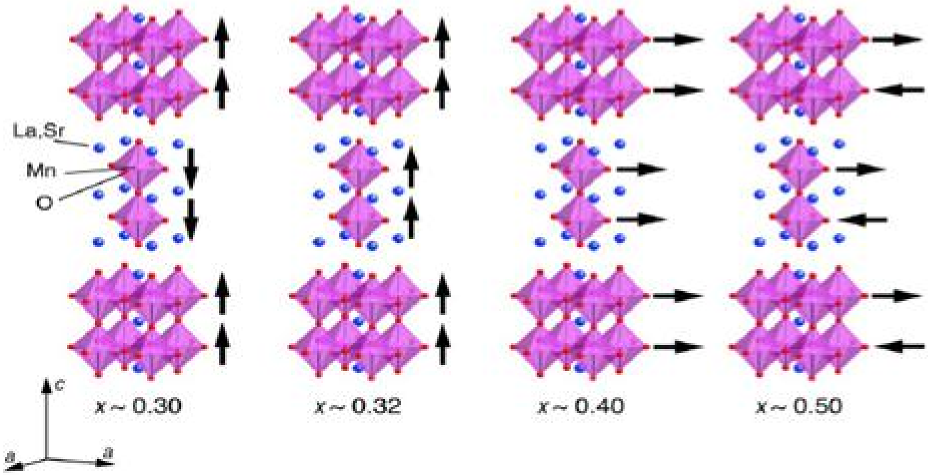

Figure 3.3: Evolution of magnetic structure in $La_{2-2x}Sr_{1-2x}Mn_2O_7$ with hole doping x [30]. The arrows represent the magnetization in a MnO_2 sheet.

$$E = K_1 \sin\theta^2 + K_2 \sin\theta^4 + K_3 \sin\theta^4 \sin\psi^2 \cos\psi^2 \tag{3.2}$$

where θ is measured from c-axis and ψ is measured from [100] direction. K_1 and K_2 are the first and second-order uniaxial anisotropy constants, and K_3 is the in-plane anisotropy constant. K_1 includes the contributions from the electronic structure K_e predominantly arising from spin-orbital coupling and the dipolar interaction K_d. K_e decreases significantly as the doping level x increases from 0.30 to 0.32 [34]. In the x=0.32 compound, K_e decreases with the temperature increasing. The dipolar energy $K_d = 2\pi D M_S^2$ ($D = 0.33$ is the dipolar sum) is around $10^6 erg/cm^3$ at low temperatures and it favors the in-plane orientation. Due to a cancelation of K_e by K_d, the first order anisotropy constant K_1

decreases dramatically with the increasing temperature and changes the sign from positive to negative around 80 K. The temperature dependence of these anisotropy constants is shown in figure 3.4. The change in K_1 and K_2 as a function of temperature indicates the easy axis of the crystal (x=0.32) may also evolve with temperature. At low temperatures, the easy axis is along the c-axis which is consistent with the magnetic ordering states determined by neutron diffraction [23]. As the temperature increases, the easy axis tilts away from the c-axis and towards the ab plane.

Recently, Asaka et al [30] observed a magnetic ripple state which evolves with temperature in zero field for the $x = 0.32$ compound by using Lorentz electron microscopy and found a spin reorientation transition occurs around 55 K to 70 K. The $x = 0.32$ compound is at the crossover from out-of-plane magnetization ($x < 0.32$) to in-plane magnetization ($x > 0.32$). Strong two-dimensional ferromagnetic fluctuations in the basal plane influence the in-plane and out-of-plane magnetization at elevated temperatures. We have conducted a systematic investigation of the evolution of ferromagnetic domains in this compound with temperature below T_C, see chapter 5.

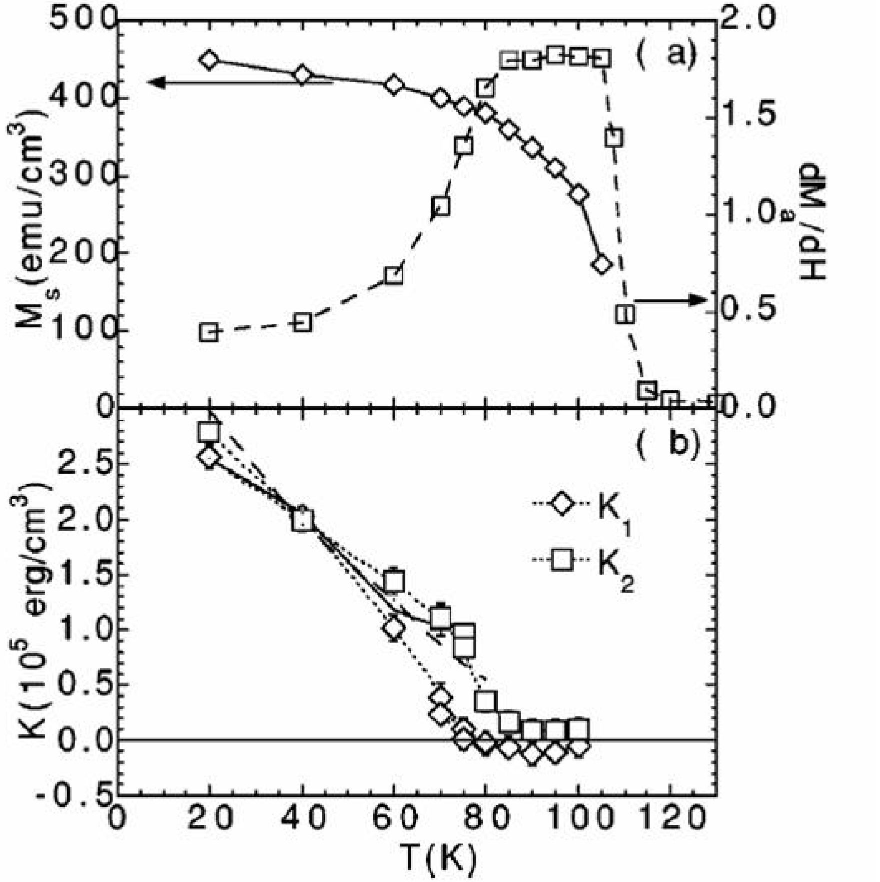

Figure 3.4: (a) Temperature vs. the saturation magnetization (left axis) and the initial susceptibility (right axis). Both were measured in the ab plane. (b) Temperature vs. the anisotropy constants K_1 and K_2. The dotted lines through the experimental data serve as guides; the solid and dashed lines represent calculated values of K_1 and K_2, respectively [34].

Chapter 4

STM Investigation of $\mathbf{La_{2-2x}Sr_{1+2x}Mn_2O_7}$ $(x = 0.32, 0.4)$

The mixed-valent manganites $R_{1-x}A_xMnO_3$ (R is a trivalent rare-earth element and A is a divalent dopant) with the perovskite structure exhibit a colossal negative magneto-resistance effect (CMR) over a certain doping region, which involves a first-order phase transition from the paramagnetic insulating state (PI) to the ferromagnetic metallic (FMM) state [35]. Manganese ions in this system take the form of high spin Mn^{3+}: t^3e^1 and Mn^{4+}: t^3e^0. The t-orbital electrons are localized with a spin S=3/2, but e-orbital electrons are at the crossover from localized to itinerant electronic behavior due to strong ferromagnetic e^1-p -e^0 interaction either via superexchange or double exchange (DE) [19] [20]. In the PI state ($T > T_C$), the spin moments at the Mn ions are not polarized, the single-electron bandwidth (W) is smaller than the effective energy U_{eff} that separates successive redox energies [36], the e-orbital electrons at Mn^{3+} ions are localized and the conduction mechanism of the system can be described as polaron hopping. In the FMM state ($T < T_C$), the spins are polarized and the strong DE interaction gives rise to $W > U_{eff}$, so that the system shows metallic behavior. The electrical transport measurement demonstrated that, upon cooling, the resistivity drops rapidly with temperature at $T < T_C$ and becomes almost independent of temperature in the low temperature region [37] [38]. The understanding of the conduction mechanism of the ferromagnetic metallic state is still unsolved. The main issue here is whether the metallic state can be described by band theory with a defined Fermi surface or by the polaron hopping theory with a very small motional enthalpy [22]. Although the theories based on strong electron and Jahn-Teller (JT) phonon coupling successfully explained the CMR phenomena [39] [40], they did not capture the main physics at low temperatures.

It is desirable to acquire the microscopic electronic structures of the CMR manganites in order to shed light on the nature of their ferromagnetic metallic state. The scanning tunneling microscope (STM) is a suitable tool to do this work since it has been successfully applied to the study of nano-sized electronic structures of other transition metal oxides (TMOs), such as cuprates [6] [41] and ruthenates [42]. We studied the bilayered manganite $La_{2-2x}Sr_{1+2x}Mn_2O_7$ ($x = 0.32, 0.4$) with a home-built LTSTM, which is described in chapter 1. The reason we chose this system is two-fold: (1) The STM is a surface sensitive tool that requires a sample with a flat and clean surface. The $La_{2-2x}Sr_{1+2x}Mn_2O_7$ has a cleavage plane between two neighboring (La,Sr)O layers due to purely ionic bonding. We can *in situ* cleave the sample to keep the surface free of contamination. (2) Compared to the three-dimensional $La_{1-x}Sr_xMnO_3$, the $La_{2-2x}Sr_{1+2x}Mn_2O_7$ exhibits stronger CMR effect with a reduced dimensionality. Reduced dimensionality enhances the fluctuation of charge, spin and orbital ordering, which leads to a more interesting change in magnetic states as a function of hole doping [30] [43].

Single crystals $La_{2-2x}Sr_{1+2x}Mn_2O_7$ were grown by the traveling melt zone method in an image furnace at the Argonne National Laboratory [1]. The resistivity curves in zero external magnetic field show that the resistivity changes very little from 80 K to 20 K and starts to turn up below 20 K [28]. The up-turn may be due to the weak electron localization effect [44]. The sample was *in situ* cleaved in the STM chamber with a base pressure of 2×10^{-10} torr or less, then immediately loaded into the sample holder which is connected to a cold finger. A mirror-like flat surface was easily obtained after the sample was cleaved due to its layered structure. Electrochemically etched Pt/Ir tips were used and cleaned *in situ* by electron beam bombardment. As for the tunneling configuration, the tip is virtually grounded, whereas the bias voltage is applied to the sample. We performed topography, single-point tunneling spectroscopy (SPTS) and current-imaging tunneling spectroscopy (CITS) measurement on $La_{2-2x}Sr_{1+2x}Mn_2O_7$ crystals (x = 0.32, 0.40) at 80 K and 20 K.

4.1 Topography with Nano-Sized Features

The weak ionic bonding between (La,Sr)O- (La,Sr)O indicates that the cleavable plane lies in between the neighboring (La,Sr)O layers. The exposed surface layer was confirmed to be the (La,Sr)O layer by X-ray photoelectron spectroscopy [45]. In most cases, the topmost layer we observed is the (La,Sr)O

---

[1] Samples were kindly provided by Dr. John Mitchell at Argonne National Lab.

layer. But we occasionally observed small-sized Mn-O layers exposed in between two large-sized (La,Sr)O layers. All of the tunneling spectra and conductance maps reported in this paper were measured on the (La,Sr)O layer. By tunneling through the exposed insulating (La,Sr)O layer, the STM probes the electronic structure of the Mn-O layer about 2 $\AA$ below the (La,Sr)O layer [23]. This is similar to the $Bi_2Sr_2CaCu_2O_{8+\delta}$ system, where the exposed layer is the insulating Bi-O, yet the STM reveals the intrinsic local density of states (LDOS) originating from the Cu-O plane about 5 $\AA$ below the Bi-O plane.

Typical STM topographic images of the x=0.4 sample taken in the constant-current mode at 80 K and 20 K are shown in figure 4.1. Nano-sized patterns shown in figure 4.1 (c), (d) indicate the existence of electronic inhomogenity, which is caused by the segregation of Mn^{3+}-rich and Mn^{4+} -rich regions within the mixed-valent matrix, formed by JT distortions and then neutralized by La^{3+} and Sr^{2+} inhomogenities [43]. In the Mn^{3+}-rich region, also called hole-poor region (HPR), the number of unoccupied states are smaller than the average because half of the e-orbitals at Mn^{3+} ions are filled, whereas in the Mn^{4+}-rich region, also called hole-rich region (HRR), the number of unoccupied states are larger than average because the two e-orbitals at the Mn^{4+} ions are empty. Because this system is doped with holes and x represents the fraction of doped holes per Mn ion, it is convenient to discuss the charge carriers in terms of holes. At a positive sample bias, the STM tip probes the density of unoccupied states. Thus, in figure 4.1 (c), (d), the bright regions are Mn^{4+}-rich and the dark regions are Mn^{3+}-rich. The average lateral

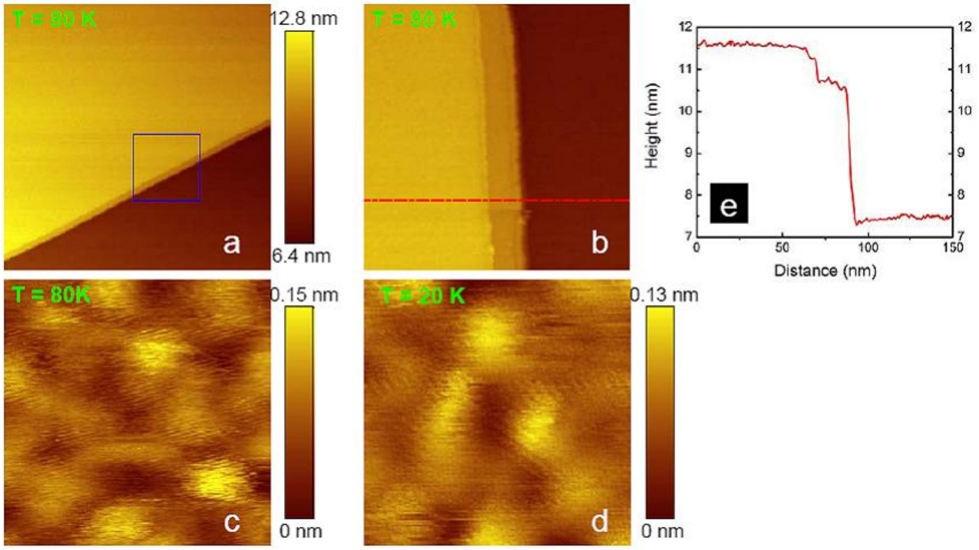

Figure 4.1: (a) A typical (766 nm)^2 topographic image, taken at 80K, showing large flat surface and steps (V_S = 0.8 V, I = 110 pA). (b) A zoom-in topographic image ((148 nm)^2) of the area enclosed by a blue square in (a). (c) (5.4 nm)^2 topographic image (V_S = 0.8 V, I = 60 pA). (d) (4.8 nm)^2 topographic image (V_S = 1.5 V, I = 100 pA). The bright region represents Mn^{4+}-rich, whereas the dark region represents Mn^{3+}-rich. (e) A line profile along the red dashed line in (b). The small step is about 10 $\mathring{A}$ high and the large step is about 30 $\mathring{A}$ high.

size of the Mn^{4+}-rich regions increases from about 1.5 nm to about 1.8 nm upon cooling from 80 K to 20 K, which may indicate the mobility of holes is reduced. Similar nano-sized patterns were also observed in the x = 0.32 sample, the lateral sizes of these Mn^{4+}-rich and Mn^{4+}-rich regions are very close to those in the x = 0.40 crystal.

Upon reversing the sample bias voltage, we would expect the contrast of the image to reverse. This is based on the STM measurements of thin film $La_{0.325}Pr_{0.3}Ca_{3/8}MnO_3$, where the topographic image of an atomic pattern containing localized Mn^{4+} and Mn^{3+} ions reversed contrast as the bias voltage changed polarity [46]. But we did not clearly observe the reversal of the contrast of the topographic images of our $La_{2-2x}Sr_{1+2x}Mn_2O_7$ crystals. Instead, as the sample bias was reversed to negative, the tunneling current became very unstable and nano-sized spots about 2 $\mathring{A}$ high were observed randomly distributed on the surface. The unstable tunneling current indicates the tunneling junction was disturbed by the slight interaction between the STM tip and sample surface due to the reduced tip-sample separation. This would be the case if the probability of extracting electrons from the sample is smaller than ejecting electrons into it, with the same tunneling current setpoint, the tip has to move further towards the sample as the sample bias changes from positive to negative. This is confirmed by the tunneling spectra shown in section 4.3.

4.2 Work Function

As shown in Eqn. 1.6 in chapter 1, the tunneling current (I_T) changes exponentially with the tip-sample separation (z) in a vacuum tunneling junction. It is very crucial to have a vacuum tunneling junction in order to probe the real local density of states (LDOS) of the sample. If the tunneling junction is not in vacuum, which would occur if the apex of the tip is covered by a layer of insulator or there is some insulating impurities located in the junction, one would observe the I_T changes almost linearly with z. A tunneling spectrum obtained through such a junction may contain the electrical transport properties of the impurities in the junction instead of showing the LDOS of the sample. Therefore, before measuring a tunneling spectrum, we check the tunneling junction to make sure it is in vacuum by measuring I_T vs. z curves. Figure 4.2 shows a I(z) curved measured at 20 K on a x=0.4 crystal.

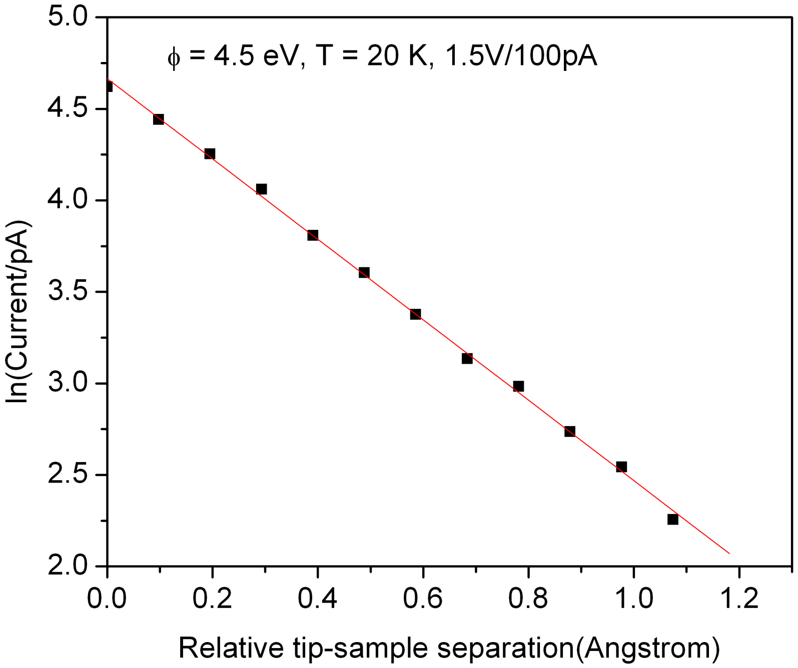

Figure 4.2: I(z) curve taken at 20 K on a x = 0.4 crystal

From an I_T vs. z curve, we can estimate the work function of the sample. We can derive the work function ϕ from Eqn. 1.6:

$$\phi \approx 0.95(\frac{d \ln I_T}{dz})^2 \tag{4.1}$$

Although Eqn. 4.1 has been successfully used to estimate work functions of metals, we must be very careful to apply this equation to a strong correlated electron system, such as $La_{2-2x}Sr_{1+2x}Mn_2O_7$. The electrons in this system are no longer bare electrons but dressed by the strong electron-electron correlation and electron-lattice coupling. But we still can have a rough idea about the work function estimated with Eqn. 4.1. By measuring I (z) curves, we calculated the average work function of the x = 0.4 crystal to be 5.5 eV at 20 K and 2.3 eV at 80 K, which agrees with the value 3.56 eV at 60 K measured by means of photoemission [47]. In the x = 0.32 compounds, the work function is a bit smaller, 4.5 eV at 20 K and 2.0 eV at 80 K.

4.3 Single-Point Tunneling Spectroscopy

In the single-point tunneling spectroscopy (SPTS) mode, I(V) curves are obtained at a fixed point and differential conductance dI/dV(V) curves are either numerically derived from the I(V)s [2] or directly obtained by using a lock-in amplifier(SR 830), see appendix C. Before taking the tunneling spectra, we routinely quantified the tunneling junction by measuring the tunneling current (I) as a function of tip-sample separation (z). A clean vacuum tunneling

---

[2] We numerically derived $\frac{dI}{dV}$(V) from I(V) curves. I(V) curves were smoothed by the Savitzky-Golay (S-G) method before taking the 1^{st} order derivative. We used 2^{nd} order S-G fitting over 21 points. Generally, one I(V) curve contains around 500 equally spaced bias voltages with a step size of 5-10 mV. The fitting window is around 100 - 200 mV. If the LDOS has some sharp peaks with the energy width less than 100 meV at certain energies, we may broaden these peaks, which we do not expect to occur. But the main features should remain unaffected.

junction indicates the tunneling current changes exponentially with tip-sample separation. All the tunneling spectra presented in this paper were obtained under a clean vacuum tunneling condition.

4.3.1 Tunneling Spectra at Mn^{3+}-rich Regions vs. at Mn^{4+}-rich Region

Figure 4.3 (a) shows the tunneling spectra taken at Mn^{3+}-rich and Mn^{4+}-rich regions in a x = 0.4 crystal at 80 K. At positive sample bias, the tunneling spectra behave similarly, whereas at negative sample bias, the tunneling spectra at the Mn^{4+}-rich region shows smaller tunneling conductance compared to the Mn^{3+}-rich region. This should be expected because the Mn^{4+}-rich region corresponds to HRR while the Mn^{3+}-rich region corresponds to HPR. Figure 4.3 (b) shows typical SPTS taken at Mn^{3+}-rich regions in an x = 0.4 crystal at 80 K and 20 K. Similar behavior was observed at Mn^{4+}-rich regions.

4.3.2 Gap Feature

As can be seen in figure 4.3, a gap appears in the tunneling spectra near the Fermi level (sample bias $V_S = 0$). To interpret this, we need to consider not only the nature of the ferromagnetic metallic state but also the role of the exposed (La,Sr)O layer in the tunneling process. As a good starting point, we compare our STM results with the ones obtained by another surface sensitive technique, angle-resolved photoemission spectroscopy (ARPES), which detects the filled states on the surface [48] [29] [49] [50].

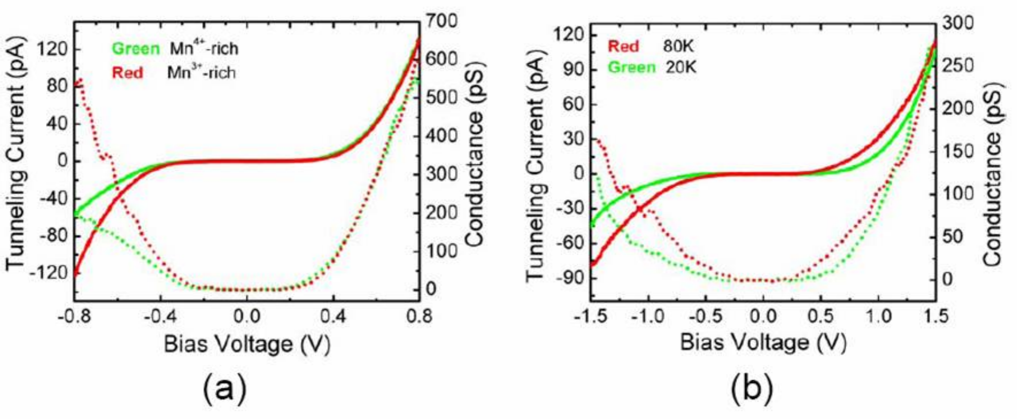

Figure 4.3: (a) Comparison of I(V) (solid line) and dI/dV (dotted line) curves taken at Mn^{4+}-rich and Mn^{3+}- rich regions at 80 K. Each I(V) spectrum was averaged over 100 I(V) curves taken within around a $(2nm)^2$ area. The tunneling junction is 0.8 V/120 pA. (b) Comparison of I(V) (solid line) and dI/dV (dotted line) curves taken at a Mn^{4+}-rich region at 20 K and 80 K. Each I(V) spectrum was averaged over 50 I(V) curves taken within around a $(2nm)^2$ area. The tunneling junction is 1.5 V/100 pA.

ARPES measurements on the $La_{1.2}Sr_{1.8}Mn_2O_7$ below T_c reveal a pseudo gap accompanied by a large 'ghost' Fermi surface and a small quasi-particle state near the Fermi level along the nodal direction, which is consistent with electrical transport measurements. [29]. On the other hand, STM measurements on the $La_{2-2x}Sr_{1+2x}Mn_2O_7$ ($x = 0.30, 0.32, 0.4$) show a large gap ($> 0.6eV$) where the LDOS completely vanishes [43] [51], which is not consistent with the ARPES results. Ronnow et al. [51] argued the gap is intrinsic to the sample and may be associated with the breakup of polaronic quasiparticles, which are analogous to the Cooper pairs in the high T_C superconductors. We believe that the gap is related to the high bias field [43]. A bias voltage higher

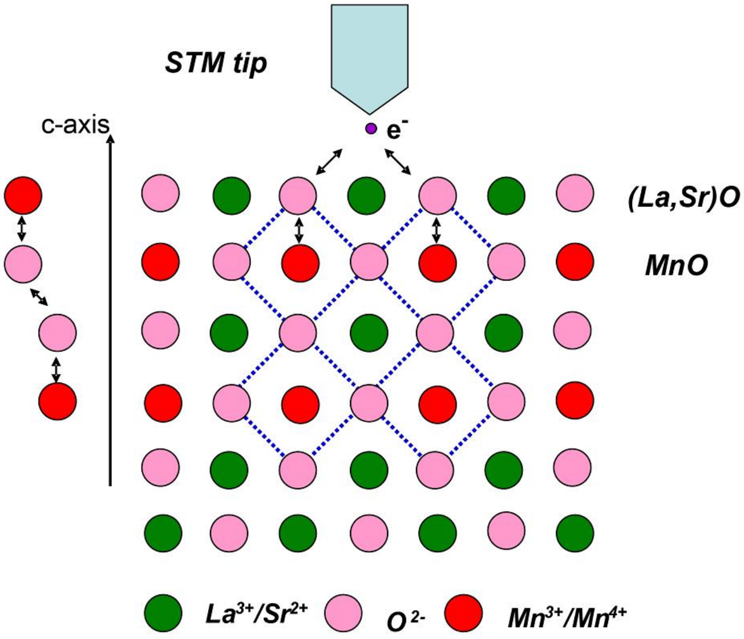

Figure 4.4: A schematic of the tunneling process occurring between the Mn-O layer and the tip through the exposed (La,Sr)O layer.

than the threshold voltage applied between the sample and STM tip induces the e-orbitals to locally reorient from in-plane to out-of -plane so as to make the e-orbital electrons locally change from itinerant to localized. In addition to this, we need to take account of the role of the exposed (La,Sr)O layer in the tunneling process. Figure 4.4 shows the tunneling process for the electrons tunneling between sample and tip. The tunneling electrons coming from the σ^*-band at the Mn-O layer have the largest probability hopping to the O^{2-} ion first then tunneling to the STM tip. Electrical transport measurements shows that conduction along the c-axis can be described as conventional small polaron hopping and that no fast electron transfer across the Mn-O-O-Mn bridge occurs [28]. This indicates that it requires energy for the electrons to hop from the Mn-O layer to the O^{2-} ion. To overcome this energy, a certain amount of bias voltage needs to be applied, which may result in a gap appearing in the tunneling spectra. But the gap size is much larger than the activation energy for small polaron motion. We attribute this to spin-disordered tunneling occurring in the Mn-O-STM-tip junction compared to spin-ordered tunneling through the Mn-O-O-Mn within the single crystal below T_C.

4.3.3 Asymmetry of Tunneling Spectra

I(V) and dI/dV(V) curves are asymmetric as a function of sample bias (V_S). The tunneling conductance is smaller at negative bias voltage than at positive bias voltage. The tunneling conductance at different bias voltages is approximately proportional to the LDOS at corresponding energies with respect to the Fermi level (E_F). The asymmetry of the I(V) and dI/dV(V) curves in figure 4.3 indicates the LDOS above E_F is larger than that below E_F. Asymmetric LDOS was also observed in copper oxides such as hole-doped $Ca_{2-x}Na_xCuO_2Cl_2$ [26] and $Bi_2Sr_2CaCu_2O_{8+\delta}$ [41]. In lightly hole-doped $Ca_{2-x}Na_xCuO_2Cl_2$, the probability of extracting electrons from the sample greatly exceeds that of injecting electrons into the sample, as expected in a lightly doped Mott insulator because there are more electrons than holes. In $Bi_2Sr_2CaCu_2O_{8+\delta}$, the markedly asymmetric DOS is a characteristic feature for high temperature superconductors that can be interpreted within the frame of the ’t-J’ model [52].

4.3.4 Hole or Electron Localization

The tunneling conductance becomes smaller at 20 K than at 80 K. To interpret this, we need to consider the temperature dependent electronic behavior of e-ortibal electrons. Below T_C, the e-orbital electrons transit from localized to itinerant due to the strong DE interaction. If all the e-orbital electrons formed a band, the Fermi level would be sitting slightly above the middle of the band because there is 0.6 electron per Mn ion. Such a picture of DOS is apparently incorrect according to the results shown in figure 4.3. We believe partial localization of e-orbital electrons may exist in this system. As the temperature goes lower, in addition to polaronic localization, Anderson localization also contributes to the decrease of the itinerant electrons. The tunneling conductance at negative bias voltages would decrease upon cooling from 80 K to 20 K, as shown in figure 4.3 (b). Thus we conclude that below T_C the localized electrons coexist with itinerant electrons in ferromagnetic $La_{2-2x}Sr_{1-2x}Mn_2O_7$ (x=0.32, 0.4), which is also confirmed by the conductance maps discussed in section 4.4 in this chapter

4.3.5 Negative Tunneling Conductance

Figure 4.5 shows negative tunneling conductance obtained in a Mn^{4+}-rich region at 80 K, which may be indicative of hole localization. We observed negative tunneling conductance only at certain Mn^{4+}-rich regions at 80 K,

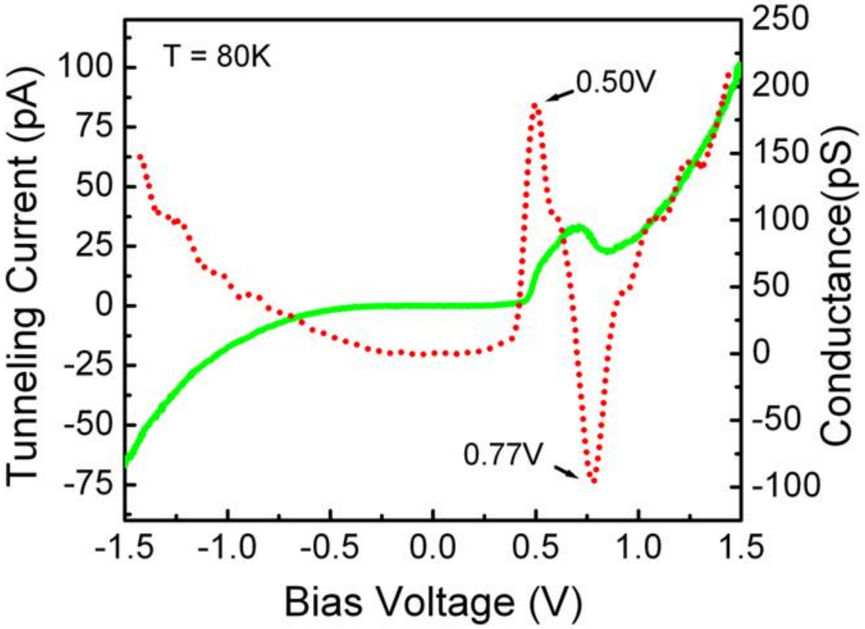

Figure 4.5: I(V) (green solid line) and dI/dV (red dotted line) taken at a Mn^{4+}-rich region at 80 K, showing negative differential conductance. The I(V) spectrum was averaged over 30 I(V) curves taken within a $(2\mathrm{nm})^2$ area.

never did at 20 K or in the Mn^{3+}-rich region. One would argue this may be due to existence of impurities in the tunneling junction, such as atoms picked from the sample, which contain resonant states. Generally, if the tip picks up atoms, such as La, Sr, O and Mn, from the sample surface, we would expect to observe abrupt changes in the topographic image and an unstable tunneling junction. In fact, we did not observe these before and after taking the tunneling spectra. We believe negative tunneling conductance may be associated with formation of two separate narrow e-orbital resonant states (d_{z^2}, $d_{x^2-y^2}$) in the

Mn^{4+}-rich regions. To qualitatively interpret this, we consider the tunneling current in Eqn. 1.2 in chapter 1 and the tunneling matrix at a high bias voltage:

$$|M(\epsilon, z, V)|^2 \propto \exp(-\alpha z \sqrt{\phi - \epsilon + \frac{eV}{2}}) \tag{4.2}$$

where z is the tip-sample separation; V is sample bias voltage; ϕ is the work function of the sample; α is a constant coefficient. In a metal-to-metal tunneling or metal-to superconductor tunneling case, an applied bias voltage is generally in the order of mV, which is negligibly small compared to the work function (usually several volts). Thus the square barrier tunneling approximation is valid. But when a high bias voltage is applied, one must consider the tilt of the square barrier. The work function measured in the x = 0.4 crystal at 80 K is 2.3 eV, see section 4.2 in this chapter. Therefore, we should consider the tunneling matrix in Eq. (2). When the Fermi level of the tip reaches the d_{z^2} resonant state by applying a bias voltage $V_1 = 0.5V$, the tunneling current is maximum. As the Fermi level moves up more towards the vacuum level by applying larger sample bias voltage, it falls in between the d_{z^2} and $d_{x^2-y^2}$ resonant states. The tunneling current reduces due to a decrease in the tunneling matrix. It becomes a minimum right before the Fermi level reaches the resonant $d_{x^2-y^2}$ state at $V_2 = 0.77V$. $\Delta = e(V2 - V1) = 0.27eV$ is the energy difference between The d_{z^2} and $d_{x^2-y^2}$ resonant states, which is close to the value of 0.4 ± 0.2 eV measured by X-ray absorption spectroscopy [53].

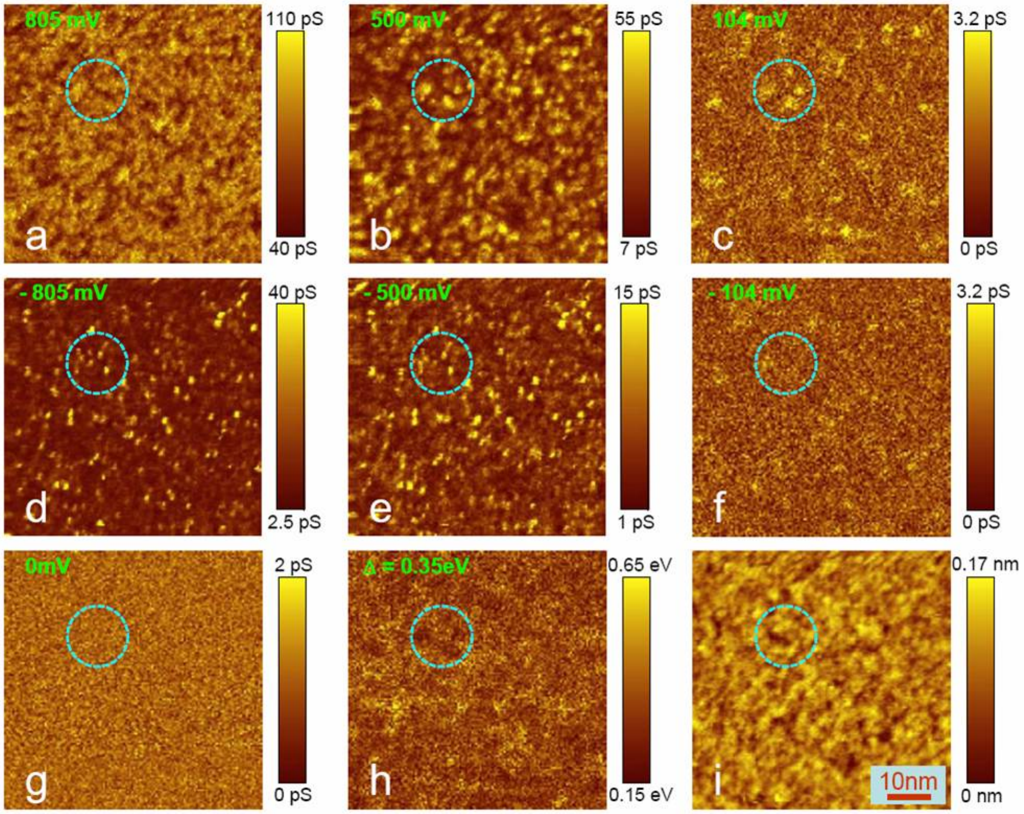

Figure 4.6: Current-imaging tunneling spectroscopy (CITS) data taken on a x = 0.4 crystal at 20 K, scan area (55 nm)^2. (a-g) are conductance maps at different sample bias voltages, numerically calculated from CITS data. (h) is a gap map, numerically calculated from CITS data. (i) is a topographic image simultaneously taken with the CITS data. The area enclosed by a guide-to-the-eye circle in each image represents the same area. The tunneling junction is 1.5 V / 100 pA.

4.4 Current-Imaging Tunneling Spectroscopy

In order to explore the spatial distribution of possible localized states, we performed current-imaging tunneling spectroscopy (CITS) measurements, which are capable of spatially resolving the LDOS [13]. In the CITS mode, the I(V) curves are taken simultaneously with the topographic images at each point, see chapter 1 for details. We tried both the IV method and the lock-in method to obtain CITS data. No significant difference was observed. In order to improve the signal-to-noise ratio while finishing a measurement within 24 hours (the STM dewars can hold a stable temperature only for maximum of 24 hours), we took as many I(V)s or $\frac{dI}{dV}s$ at each pixel as possible and then averaged them to obtain one curve.

4.4.1 Evolution of the Conductance of Mn^{3+} and Mn^{4+} Regions with Energy

Figure 4.6 shows a topographic image, seven typical conductance maps at ±800 mV, ±500 mV, ±104 mV and 0 mV and a gap map acquired over the same $(55\text{nm})^2$ scan area. According to these conductance maps, we can discuss the evolution of LDOS with bias voltage, or energy with respect to the Fermi energy.

At opposite sample bias voltages, the patterns of LDOS are completely different, see figure 4.6 (a-f). At positive sample bias, the averaged LDOS is high and some regions show relatively higher LDOS than the background, which indicates existence of localized holes. These regions with high LDOS are still distinguishable from the background even when the sample bias voltage falls into the gap region (on average, -0.19 eV to 0.16 eV), see the area enclosed by a cyan dash-line circle in figure 4.6 (c). At negative sample bias, the averaged LDOS is small; some regions with smaller lateral sizes exhibit much higher LDOS than the background. To discuss in more detail the change of the LDOS as a function of the bias voltage, we compare the LDOS over the same small area (enclosed by a cyan dashed-line circle) in each image. The topographic image, figure 4.6 (i), shows that the area enclosed by the cyan circle contains Mn^{3+}-rich (dark) and Mn^{4+}-rich (bright) regions. At high sample bias, both regions show very high LDOS, figure 4.6 (a). As the sample bias reduces to 500 mV, figure 4.6 (b), the LDOS in the Mn^{4+}- rich region becomes apparently larger than in the Mn^{3+}-rich region. Even in the gap region, figure 4.6 (c), these regions are still distinct from the background. As the bias reduces more, these Mn^{4+}-rich and Mn^{3+}-rich regions vanish into the background, figure 4.6 (g). At negative sample bias, the smaller sized spots showing higher LDOS appear in both regions, which indicates electron localization occurs in both Mn^{3+}-rich and Mn^{4+} -rich regions. As the sample bias increases towards negative values, the pattern of these spots do not change much but the background conductance increases. The conductance maps demonstrate that electron and hole localization occurs in the itinerant electron background.

Figure 4.6 (h) is a gap map, where the gap size at each pixel is expressed in terms of color contrast. It is very difficult to precisely define the gap size because the gap is not sharp enough. In this paper, we define the gap as region near zero bias voltage within which the tunneling current is less than 1 pA. The noise level of our STM system is around 1 pA. So we chose 1 pA as a threshold tunneling current value to define the gap. Due to the different definitions of the gap [51], the gap sizes may also be different. The averaged gap size shown in figure 4.6(h) is 0.35 eV, whereas the gap size varies from 0.15 eV to 0.65 eV at different locations, which indicates the gap is spatially inhomogeneous.

Freeland et al. [54] argued, based on their X-ray resonant magnetic scattering and polarization-dependent absorption measurement and corresponding theoretical simulation, that the outermost 1 nm thick layer exhibits no long-range ferromagnetic order so that the surface shows an insulating behavior. They also used the point-contact method to confirm that a 1 nm thick layer is insulating. We believe that the topmost layer should not be completely insulating, otherwise no tunneling current would be observed; the magnetism in the surface layer may be different from the one inside the crystal due to surface effects [55], but how the surface conductivity is affected by the surface magnetism still needs further investigation. It would be a good idea to do more STS investigation on this system at high external magnetic fields to observe how the LDOS evolves with magnetic fields.

4.4.2 Evolution of Charge Density Waves with Energy

Short-range charge density wave (CDW) fluctuations are very common to a quasi-two-dimensional system, such as $La_{2-2x}Sr_{1+2x}Mn_2O_7$. A crystal structure modulation can occur to lift a nesting-related degeneracy as a result of the Fermi surface nesting and strong electron-lattice coupling. Theoretical calculations based on different models predicted that the $x = 0.32, 0.4$ compounds possess nested Fermi surface [56], which was later confirmed by ARPES measurements [29] [48] [50]. The nested Fermi surface topology indicates a possible existence of charge density waves. Campbell et al. observed short-range polaron correlation with wave vector $q = (0.3, 0, \pm 1)$ at $T > T_C$ by using X-ray diffraction and neutron scattering [57]. Below T_C, the correlated polarons formed in the PI state should melt as the electrons trapped by lattice distortion are gradually released and can move freely with the help of a strong DE interaction [58]. But due to the existence of electronic inhomogeneity in this system, as we discussed in section 4.1 in this chapter, charge density waves may still appear locally at $T < T_C$. In fact, we clearly observed a 16 $\AA$ modulation in conductance maps of the $x = 0.32$ compound at 20 K., which is consistent with the CDW modulation with a wave vector about 13 $\AA$ predicted by ARPES measurement [50]. After finishing the STM measurement, we took the sample out of the chamber and performed Laue X-ray back diffraction to obtain the crystal directions. We found the static CDW propagates along a-axis.

Figure 4.7 shows that the conductance modulation, CDW, appears very clearly at high negative sample bias (energy below E$_F$), disappears gradually in the gap region and appears again weakly at high positive sample bias (energy above E$_F$). This modulation may be partially associated with the static JT

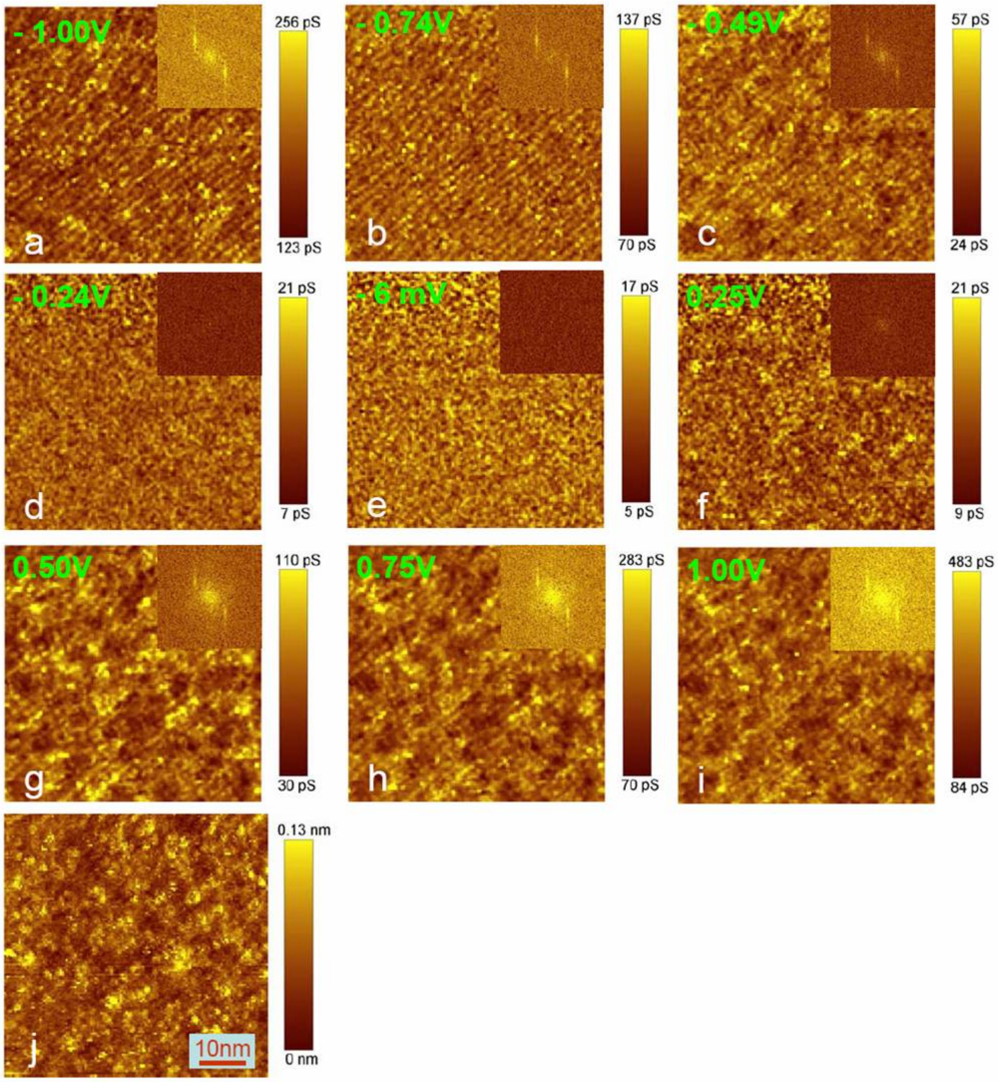

Figure 4.7: Evolution of a charge density wave (CDW) with energy. (a-i) are conductance maps at different bias voltages; the inset in each image is its corresponding fast-Fourier-transform image. (j) is the topography simultaneously taken with the conductance maps. The topography was taken at -1.0 V and 80 pA. The conductance maps were taken with a lock-in amplifier (modulation frequency 718 Hz, amplitude 15 mV)

distortion.

4.5 Possible STM Tip Effect and Artificial Defects on the Surface

The STM probes the LDOS of the sample surface. Generally, in a single crystal sample, where the atoms are located, there are high LDOS. Thus the positions containing high LDOS are related to the occupation of atoms. By following this, we are able to acquire the atom-resolved topographic image of the surface, although there are notable exceptions.

In TMOs, chemical element substitution introduces into the parent compounds charge carriers, lattice distortion and atom disorder. Strong lattice distortion and atom disorder are believed to disturb the atomic pattern on the sample surface. For example, in $Bi_{2-x}Pb_xSr_2CaCu_2O_{8+\delta}$ [59], the disorder introduced by substitution of Pb for Bi weakens and strongly perturbs the atomic pattern of the Bi-O layer. In $La_{2-2x}Sr_{1+2x}Mn_2O_7$, below T_C, the JT distortion developed in the paramagnetic state above T_C still locally exists [60] [61]. Furthermore, nano-sized inhomogeneities of La^{3+} and Sr^{2+} may occur in this system, as was observed in lightly doped $La_{1-x}Sr_xMnO_3$ [62]. Therefore, we may not be able to resolve atomic patterns. In fact, we observed nano-sized Mn^{3+}-rich and Mn^{4+}-rich regions.

It turns out that we have difficulty ruling out the STM tip effect on the topographic images. In the constant-current mode, the STM topographic image is a convolution of the tip and sample topography. If the tip is not atomically sharp, the acquired topographic image of the sample will exhibit the tip effect, such as broadened features in addition to its intrinsic topography. It is very difficult to tell the sharpness of the tip unless atomic patterns of the sample are resolved. Among numerous topographic images obtained from the single-crystal $La_{2-2x}Sr_{1+2x}Mn_2O_7$, we need to pick the images which truly represent the intrinsic electronic structure. Depending on the reproducibility of the images and finest features appearing in the images, we believe that the topographic images shown in figure 4.1 (c) (d) represent the intrinsic electronic properties of the sample. On the other hand, we can examine the cleanness of the vacuum tunneling junction by measuring the I(z) curves. A clean vacuum tunneling junction rather than an atomically sharp tip is necessary to probe the intrinsic electronic structures of the sample by tunneling spectroscopy.

We occasionally observed unknown particles appearing on some part of the sample surface, figure 4.8. Those particles are around 1.5 $\mathring{A}$ high and 1-3 nm in diameter. They can not be purely electronic features, such as HPRs, because the corrugation originating from LDOS inhomogeneity generally does not exceed 1 $\mathring{A}$. We also rule out the possibility that they are adsorbates according to: (1) the base pressure is less than 2×10^{-10} torr; the sample stays even at lower pressure due to cryogenic pumping. (2) the exposed ionic (La,Sr)O layer contains no dangling bonds to attract molecules from the environment. Therefore those particles are mostly likely to be artificial defects created during sample cleaving, such as ionic molecular clusters.

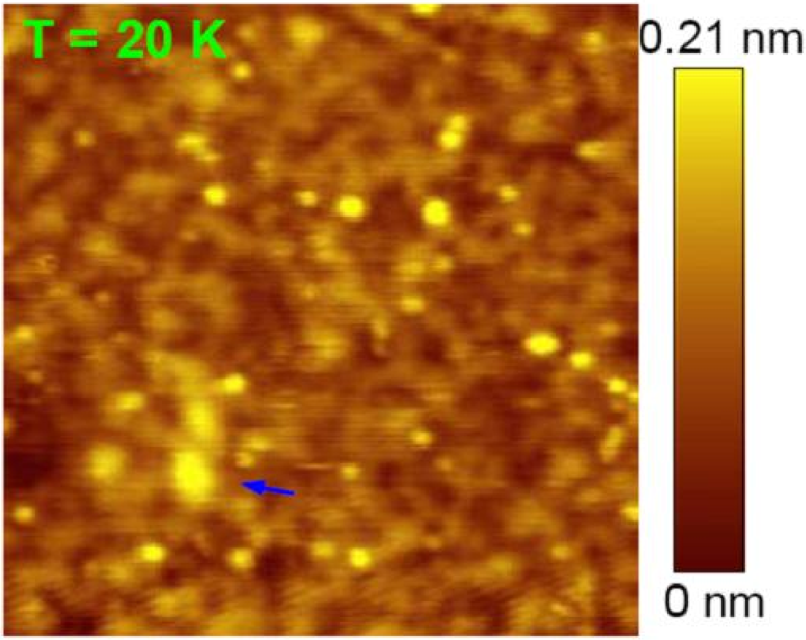

Figure 4.8: A (23 nm)^2 topographic image showing artificial particles (pointed by a blue arrow), V_S = 1.5 V, I = 100 pA.

4.6 Conclusions

We performed low temperature STM studies on bilayered single-crystal $La_{2-2x}Sr_{1+2x}Mn_2O_7$ ($x = 0.32, 0.4$). Although the top Mn-O layer carrying localized or itinerant charge carriers is around 2 $\mathring{A}$ below the exposed ionic oxide (LaSr)O layer, the STM probes the LDOS originating from the Mn-O layer by tunneling through the insulating (LaSr)O layer. The topographic images show nano-sized segregated HPRs and HRRs, which are intrinsic to the crystal and caused by JT distortion at Mn^{3+}ions and neutralized by the inhomogeneity of La^{3+} and Sr^{2+}. We discussed about the additional origin of the gap appearing in the tunneling spectra ($I(V)\&dI/dV(V)$). Besides reflecting the crossover from itinerant electron to localized electron induced by high bias fields [43], the gap is associated with the small polaronic conduction along the c-axis of the crystal. Asymmetry of the tunneling spectra indicates the coexistence of itinerant and localized electrons or holes, which is further confirmed by spatially resolved tunneling spectra, i.e. CITS. The conductance maps demonstrate the evolution of the LDOS as a function of energy with respect to the Fermi level. High localization of electrons becomes evident at high negative bias voltage. The regions showing high LDOS are still distinct from the background even within the gap region, which may be consistent with the existence of quasi-particles in the nodal direction near the Fermi level observed by ARPES [29]. A CDW caused by Fermi surface nesting and a static JT distortion was observed. It propagates along the a-axis with a wave vector of 16 $\AA$. We also discussed the possible artificial effect on the electronic structure of the sample surface exerted by the STM tip and sample cleaving. Due to the spin-dependent conduction mechanism that dominates in CMR manganites, one would naturally believe that the magnetic domain structures [30] influence the electronic structures. For example, the electronic structures in the magnetic domain walls would differ from inside the magnetic domain. Because we used normal Pt/Ir tips, we could not observe this difference. A spin-polarized STM [63] is necessary to explore the correlation between electronic and magnetic structures in CMR-manganites.

Chapter 5

Ferromagnetic State of $La_{2-2x}Sr_{1+2x}Mn_2O_7$ Probed by MFM

The formation of magnetic domains in ferromagnetic materials is a consequence of various competing energy terms, such as magnetostatic energy, magnetoelastic energy, exchange interaction and crytal anisotropic energy [64]. In a mixed-valent perovskite manganite, upon cooling through the Curie temperature, ferromagnetic (FM) domains first form into individual clusters, and then they merge together and form a percolative path through the whole sample [65]. This process relies sensitively on the relative spin orientation of neighboring magnetic domains which can be controlled by an external magnetic field. As the FM domains percolate through the whole sample, a tremendous drop in resistance can be observed, signaling a first-order phase transition from insulating to metallic behavior. Magnetic force microscopes (MFMs) have been successfully used to study the evolution of the FM domains and domain walls in the perovskite manganite with external magnetic field and temperature, and to investigate the microstructure of these domains and domain walls [66] [67].

As another type of colossal magnetoresistive manganite, the bilayered manganites $La_{2-2x}Sr_{1+2x}Mn_2O_7$ exhibit a variety of magnetic ground states as a function of the hole doping x, which originates from the intra-layer exchange interaction dominating the inter-layer exchange interaction [23], see figure 3.3. The crystal with x=0.32 possesses a ferromagnetic ground state at low temperatures with the magnetization along the c-axis. The domain structures in this compound were found to undergo a rapid change as the external parameters (pressure, temperature and magnetic field) change [24] [30] [34]. Welp et al. [34] observed maze-shaped domains in the ab plane by using magneto-optical imaging while Asaka et al. [30] observed a magnetic ripple state in this compound by using Lorentz transmission electron microscopy (LTEM). The resolution of MFM is in between that of LTEM and magneto-optical imaging. By using MFM, we can image an out-of plane domain with a lateral size down to 50 nm and an in-plane domain with a lateral size about 100 nm. We can also play with temperature and external magnetic fields. By using home-built low temperature MFM, we have investigated the evolution of magnetic domain structures with temperature and external magnetic field in this crystal.

5.1 Introduction to Magnetic Force Microscopy

Magnetic force microscopy (MFM) was developed on the base of atomic force microscopy (AFM) [68]. It belongs to the family of scanning probe microscopy. Compared to scanning tunneling microscopy (STM) discussed in chapter 1, the MFM uses a magnetic tip to probe the magnetostatic force generated by magnetic domains in ferromagnets. It uses feedback electronics and data collecting techniques similar to those of the STM.

As a magnetic tip is placed within one hundred nanometers away from a magnetic domain, the tip will feel a magnetostatic force. Assuming the effective size of the magnetic tip is small enough compared to the spatial variation of the stray magnetic field **B** generated by the domain and the tip moment **m** is parallel to the z direction, the magnetostatic force can be expressed as:

$$\mathbf{F} = -\nabla U = \nabla(\mathbf{m} \cdot \mathbf{B}) = m_z \nabla B_z = m_z \frac{\partial B_z}{\partial z} \hat{z} \tag{5.1}$$

This force causes a mechanical deflection of the cantilever where the magnetic tip is mounted. The deflection can be measured by using different techniques, such as fiber-optical interferometer [69] and piezoresistive cantilever [70]. In addition to the magnetostatic force, there are two other major forces existing between a magnetic tip and a sample, namely the van de Waals force and the electrostatic force. The van de Waals force dominates the other two forces in a short range, within about 1 nm tip-sample distance. It is utilized to obtain topographic images of the sample. The electrostatic force, a long-range force, arises from the tip and sample potential difference, so that it can be used to image the surface potential and electric dipoles.

For technical reasons, it is not the magnetostatic force itself but its gradient that is measured in an MFM mode. When the cantilever oscillates at its free resonant frequency f_0, it undergoes a frequency shift as it feels a magnetic force gradient in the vicinity of a magnetic domain. The resonant frequency under the field is given by [71] :

$$f = f_0\sqrt{1 - \frac{F'_z}{k}} \approx f_0(1 - \frac{F'_z}{2k}) \tag{5.2}$$

where $F'_z = \frac{\partial F}{\partial z}$, k is the spring constant of the cantilever, and $k \gg F'_z$ is assumed. By substituting Eqn. 5.1 into Eqn. 5.2, one can have the frequency shift:

$$\Delta f = f - f_0 = -\frac{f_0 m_z}{2k}\frac{\partial^2 B_z}{\partial z^2} \tag{5.3}$$

Eqn. 5.3 shows that the resonant frequency shift is proportional to the magnetostatic force gradient. A phase locked loop is used to measure the frequency shift of the cantilever. In MFM mode, after a scan line for the topography is finished, the cantilever oscillating at f_0 is lifted several tens of nanometers above the sample so as to eliminate the effect coming from the van de Waals force. Meanwhile, a bias voltage may be applied between the tip and sample to balance the potential difference between them so that the topographic coupling to the MFM image will be minimized. The tip either traces the topography of the sample at a pre-defined lift height or scans at a constant height in a straight line. The magnetic signal is recorded in terms of the frequency shift.

Figure 5.1 explains how the resonant frequency of the cantilever shifts in response to the stray magnetic field generated by magnetic domains. A repulsive magnetic force gives rise to a positive frequency shift while an attractive force gives rise to a negative frequency shift. In an MFM image, the contrast of the image represents the magnetization of the domains. Imaging an in-plane domain always results in a bump-and-dip frequency shift profile, while imaging an out-of-plane domain results in either a bump or a dip depending on the magnetization of the domain with respect to the tip moment (dip → parallel; bump → antiparallel). As domains rotate upon the influence of an external field, the frequency shift profiles will also change, see figure 5.1 (c) (d). An external field is often used to confirm the magnetization of the domains.

5.2 Spin Reorientation Transition

By using Lorentz transmission electron microscopy Asaka et al. [30] observed that a temperature-induced spin reorientation transition (SRT) occurs in the x = 0.32 compound. They proposed a model to interpret the evolution of the magnetic domain structure with temperature, see figure 5.2. As $T < 50K$, the magnetic domains are oriented along the uniaxial easy axis, c-axis, with a typical 180^0 domain wall structure. As the temperature increases past 50 K, a small portion of the magnetic moments begin to fluctuate. They grow into nano-sized magnetic domains with a component deviating from the c-axis. With increasing temperature, those fluctuating domains develop into domains oriented in-plane, which indicates that the easy axis of these newly developed domains changes from the c-axis to the in-plane direction. The in-plane domains coexist with the out-of plane domains from 50 K to 55 K. Above 55 K, platelike nano-sized domains form and the magnetization completely turns towards the ab plane. Those platelike nanosized domains begin

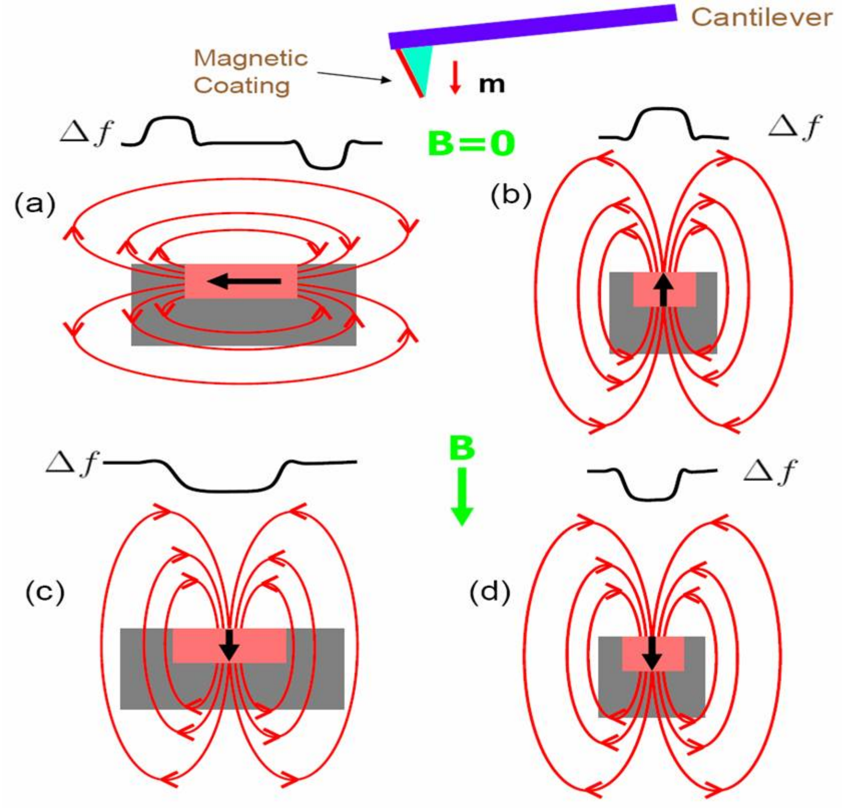

Figure 5.1: Schematic of frequency shift of a cantilever in response to magnetic domains. The tip is coated with a thin layer of magnetic material ($\sim$ 50 nm Co/Cr in our experiment). The tip is magnetized approximately along the pyramid by a strong permanent magnet. (a),(b) show the frequency shift profiles of an in-plane and an out-of plane domain at a zero field. (c),(d) show the domains rotate under an external field and the frequency shift profiles also changes.

to evolve with temperature from 55 K to 70 K. They attributed the SRT to the two-dimensional ferromagnetic moment fluctuation and the orbital occupancy transition from $d_{3z^2-r^2}$ to $d_{x^2-y^2}$.

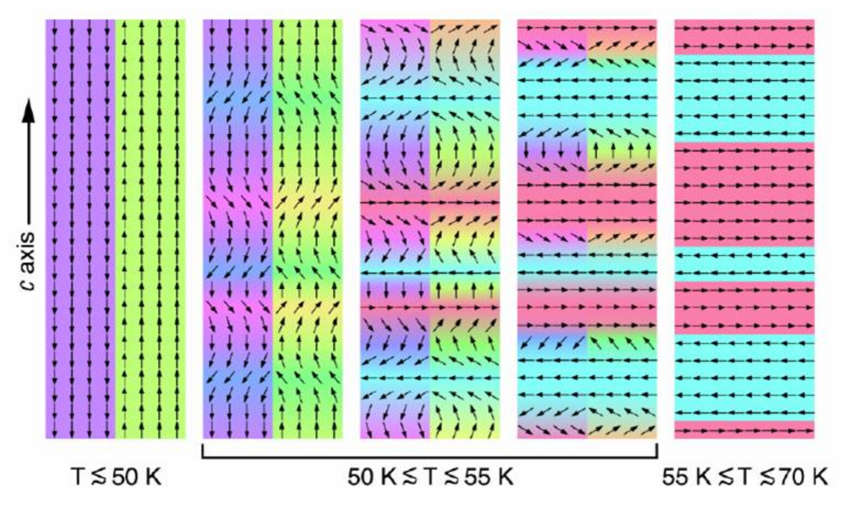

Figure 5.2: Schematic of spin reorientation transition model in $La_{2-2x}Sr_{1+2x}Mn_2O_7$ (x = 0.32) [30]. The local magnetic moment is represented by arrows. Below 50 K, the spin moment is out-of-plane. SRT occurs at 50 K to 55 K. Above 55 K, the spin moment lies down in the ab plane.

5.3 Our MFM Results

We performed a systematic MFM measurement on the x = 0.32 sample from 30 K to 110 K (T_C) under different external magnetic field conditions in order to explore the dynamic evolution of ferromagnetic domains with temperature and magnetic field. Interestingly, we obtained some new results about the domain formation at various temperatures. We may need to modify the

SRT model in figure 5.2 in order to have a better understanding of the interplay between the spin moment and the orbital degrees of freedom.

5.3.1 Evolution of Magnetic Domains with Temperature

The sample was first zero field cooled down to 30 K and then warmed up to 80 K. The MFM images were taken in a warming up run. Figure 5.3 shows the evolution of the magnetic domains with temperature from 30 K to 80 K. Figure 5.3 (g) is the topography where MFM images (a)-(f) were taken. At 30 K, magnetic domains form treelike patterns with a 180^0 domain wall structure. The width of the domains arranges from 200 nm to 500 nm. The magnetization of the domains is out-of-plane. Bright and dark areas are domains with magnetization pointing out of and into the sample respectively. Such a magnetic domain structure commonly appears in uniaxial ferromagnets, such as on the hexagonal closed packed cobalt (001) surface [72] [73]. The formation of these magnetic domain patterns can be interpreted by considering the energies associated with the surface free magnetic poles and the domain walls [74]. The magnetostatic energy gain due to reducing the separation of these domain walls is balanced by the domain wall energy loss due to increasing the total area of domain wall. With the temperature increasing from 30 K to 65 K, the domain patterns remain stable but the magnetization of the domains gradually reduces as to be expected from a Brillouin function [75] (note the scale bars in figure 5.3), but no in-plane domains are apparently observed. The domain walls start to show a visible movement at 74 K (refer to the middle of

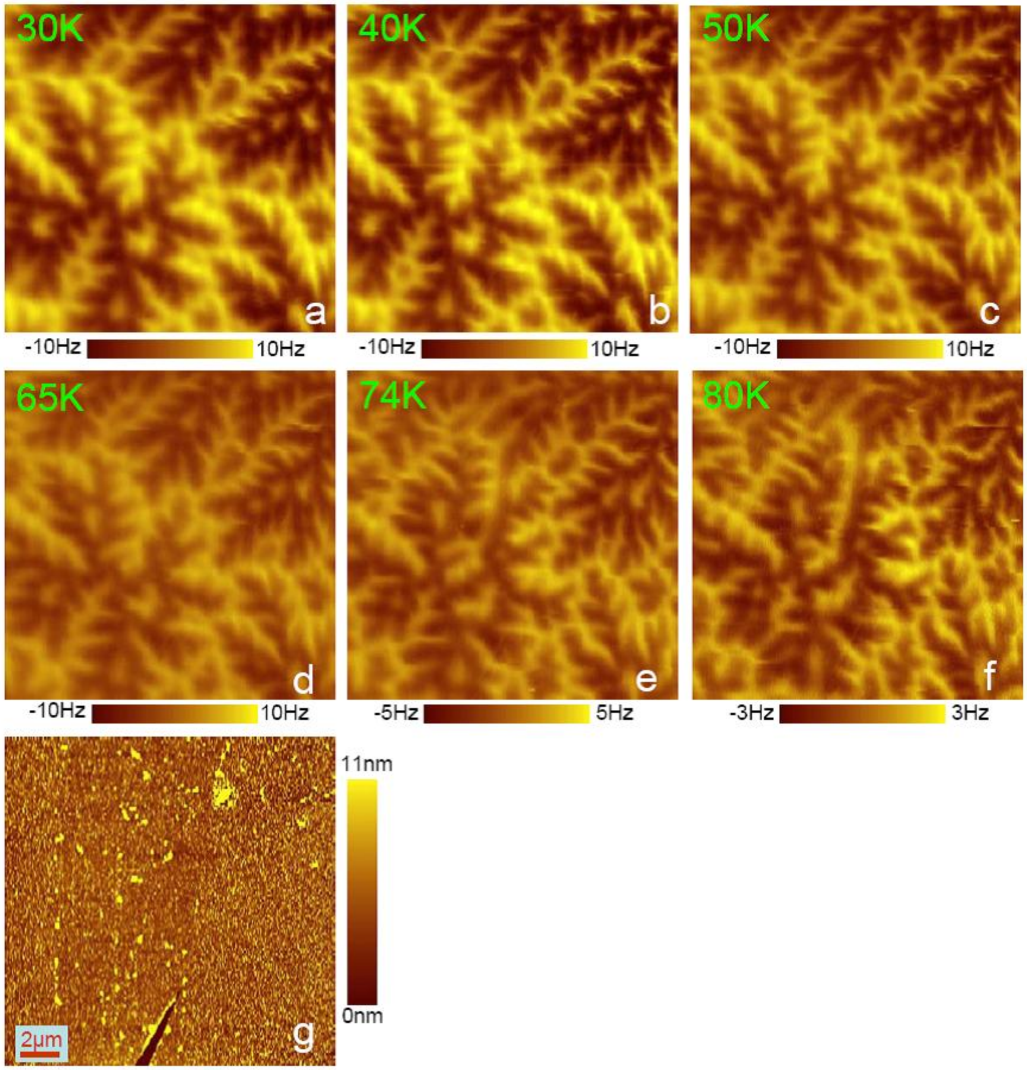

Figure 5.3: Evolution of ferromagnetic domains with temperature. (a)-(f) are MFM images taken at the same position at zero field. (g) is the topography with size $18\mu m \times 18\mu m$.

the MFM images), which indicates that the old balanced state breaks down and a new balanced state shows up. The motion of domain walls is dominantly caused by the competition between the surface magnetic free pole energy and domain wall energy. It may be partially driven by the change in the easy axis direction or by the two-dimensional ferromagnetic fluctuation in the basal plane. This is aslo indicative of the onset of the SRT.

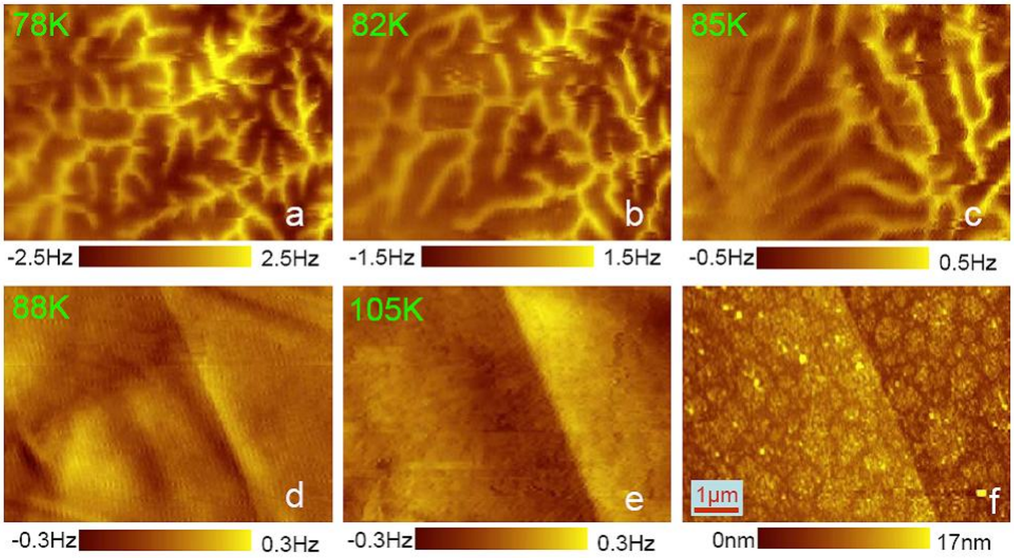

Figure 5.4: (a)-(e) are MFM images taken at the same area shown in (f) at zero field. (f) is an $8\mu m \times 6\mu m$ topography.

As the temperature increases more, the domain motion becomes more and more rapid, figure 5.3(f). Above 80 K, we started to take MFM images with smaller temperature steps in order to obtain a detailed picture of the dynamic evolution of the spin moment with temperature. Figure 5.4 shows a series of MFM images taken in a warming up run. These MFM images were taken at a different position from those shown in figure 5.3. As the temperature increases from 78 K to 85 K, figure 5.4(a)-(c), we can see that the small wavy domains merge into larger domains at elevated temperatures; curved domain walls change their stretching directions on the surface in such a manner that they tend to form parallel stripes. As we know, the domain width is approximately proportional to $\frac{\sqrt{\gamma}}{M_s}$ (γ is domain wall energy per unit area, M_s is magnetization) [75]. Since the domain wall energy and the magnetization change with temperature, the domain width changes with temperature as well. Below 88 K, the major component of the magnetization is still out-of plane. As the temperature is raised up to 88 K, the in-plane domains dominate while all the out-of plane domains disappear. This signals that the SRT finishes around 88 K in this sample. Those in-plane domains become weaker and weaker at higher temperatures until they disappear around the Curie temperature, as expected.

In CMR-manganites, the formation of ferromagnetic domains is correlated with the change in resistivity. Transport measurement on the x=0.32 compound shown [24] that the resistivity along the c-axis and in the ab plane remains almost constant below 60 K. At low temperatures, the resistivity exhibits a slight upturn, which indicates charge localization or short-range charge ordering. The resistivity gradually increases from 60 K to 100 K and it exhibits a sudden increase near the Curie temperature 110 K due to a metal-insulator transition. Our MFM measurement shown that the ferromagnetic domain patterns remain very stable below 60 K, which is correlated with nearly constant resistivity. The domains start to move with the magnetization remaining out-of-plane as the temperature increases from 60 K to 88 K, which corresponds to the gradual increase in resistivity. Above 88 K, the magnetization of the domains tilts away from the out-of-plane direction and towards the in-plane direction, signaling the change in the direction of the easy axis. This doest not occur in three-dimensional CMR-manganites such as $La_{1-x}Ca_xMnO_3$ or $La_{1-x}Sr_xMnO_3$. Due to the two dimensionality of $La_{2-2x}Sr_{1+2x}Mn_2O_7$, the first order crystal anisotropy constant of the x=0.32 compound changes sign near 80 K [34], which results in the change in the direction of the easy axis. Detailed dynamic evolution of domains with temperature above 88 K can not be obtained with our MFM because of the complexity of those in-plane domain patterns.

Another interesting result we observed in the sample is thermal hysteresis showing in the MFM images. The thermal cycle started at 78 K, increased to 82 K and came back to 78 K. MFM images were taken at initial 78 K and finial 78 K at the same position. We found the magnetic structure depends on the thermal history, see figure 5.5. Figure 5.5 (a) was taken at 78 K after the sample was zero field cooled down. Figure 5.5 (b) was also taken at 78 K but after the sample experienced a thermal cycle (78 K → 82 K → 78 K). Comparing Figure 5.5 (a) to (b), we can see that the domain patterns are significantly different and the domains with stronger magnetization (brighter areas at the upper left part of the images) underwent less changes than the weaker domains. The thermal cycle dependence of magnetic structure at the nanoscale

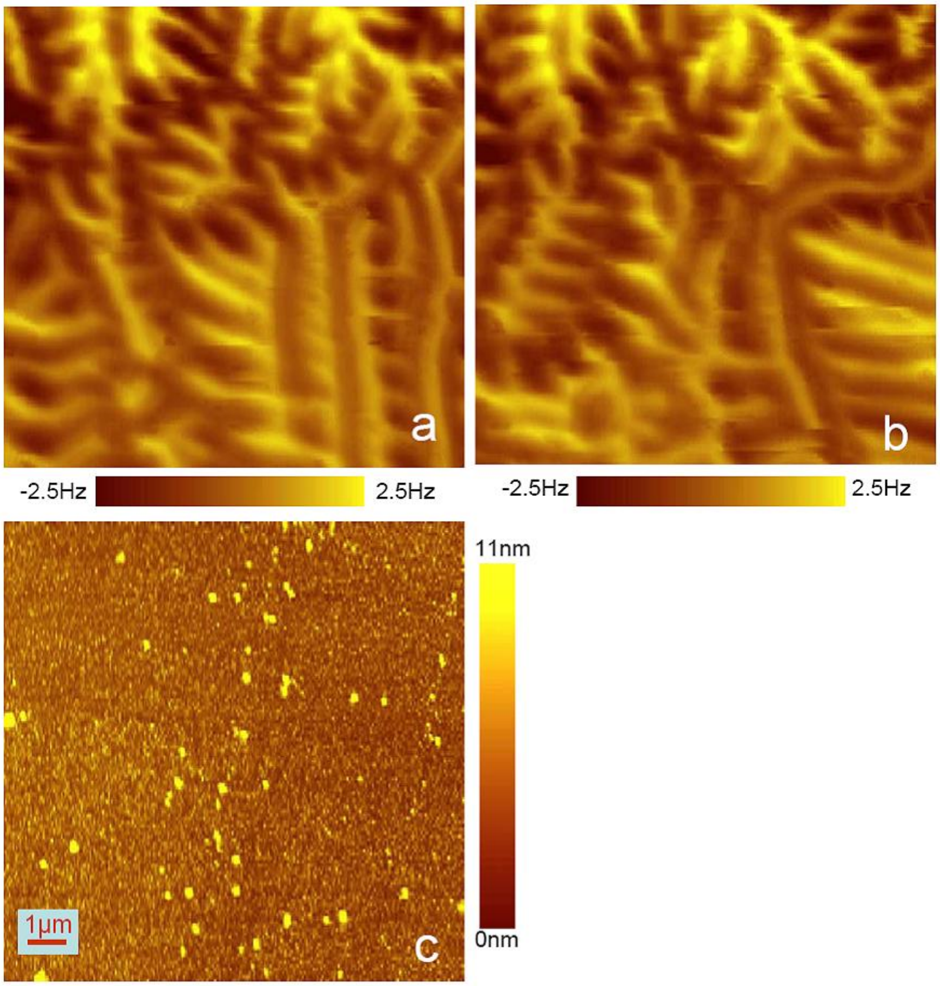

Figure 5.5: Thermal hysteresis observed in the magnetic structure. (a) is an MFM image taken at initial 78 K. (b) is an MFM image taken at final 78 K. (c) is a $10\mu m \times 10\mu m$ topography.

in this compound has not been reported so far. This is evidence of the existence of strong competition between magnetostatic energy and domain-wall energy nearby 80 K and the existence of possible temperature-assisted two-dimensional spin fluctuations.

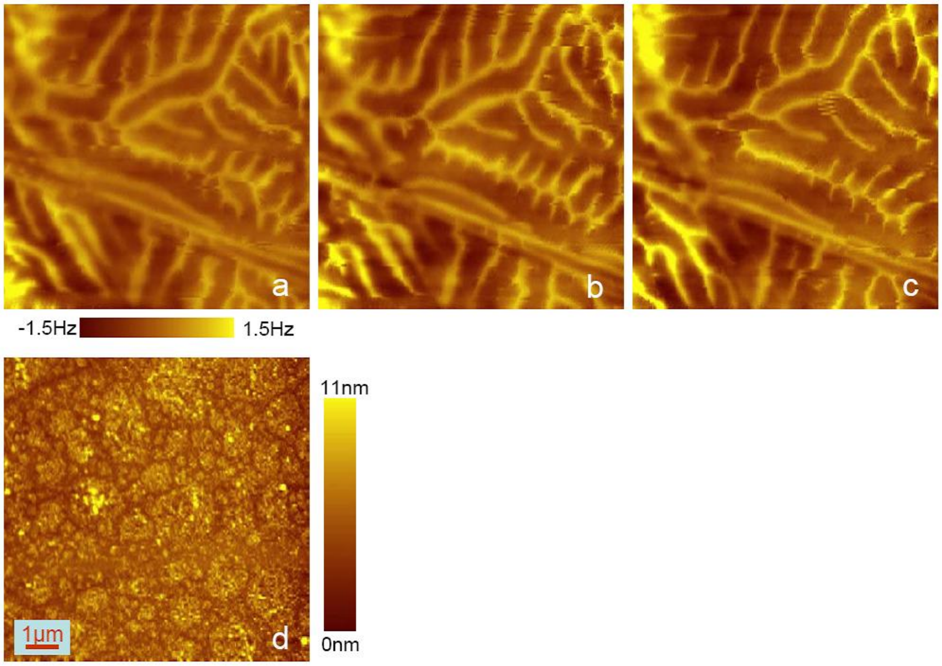

Figure 5.6: The MFM images were taken at 78 K in a field increasing run. (a)-(c) are MFM images taken at different fields. (a) zero field. (b) 60 Gauss. (c) 185 Gauss. (d) is an $8.6\mu m \times 8.6\mu m$ topography where MFM images (a)-(c) were taken.

5.3.2 Evolution of Magnetic Domains with Magnetic Field

MFM can qualitatively measure the magnitude of the magnetic force gradient and identify the magnetization direction of domains. It is difficult to quantitatively measure the amount of in-plane component or out-of-plane component of the magnetization. The magnetic tip is generally magnetized along the tip pyramid. Given the sizes of domains and the tip geometry, MFM would be more sensitive to out-of-plane magnetic domains than in-plane ones. When studying a magnetic sample with in-plane domains, we may apply a sufficient large external field to make the domains rotate from in-plane to out-of plane so that we can study the domain structure from a better angle.

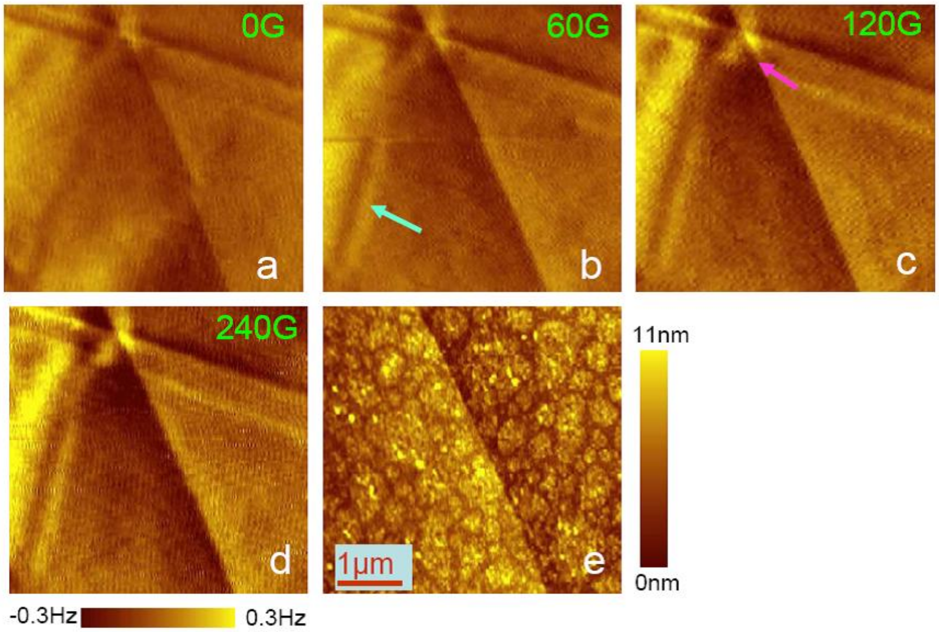

Figure 5.7: The MFM images were taken at 88 K in a field increasing run. (a)-(d) are MFM images taken at different fields. (e) is a $7.3\mu m \times 6.9\mu m$ topography where MFM images (a)-(d) were taken.

In the presence of external magnetic fields, we measured the magnetic domain structure in the sample at 78 K and at 88 K, see figure 5.6 and figure

5.7. The field is applied perpendicular to the sample surface along the tip magnetic moment. Figure 5.6 (b) was taken with 60 Gauss applied, and we see that the magnetic structure changes slightly in the form of domain wall motion. No apparent domain rotation can be observed. When the field is increased up to 185 Gauss, the growth of the domains parallel to the field is enhanced, which results in the increase in the dark area and decrease in the bright area. We believe the main component of the magnetization is still out-of-plane at 78 K. At 88 K, the MFM image in figure 5.4(d) shows the magnetization of most domains is in-plane. Upon applying external fields, the in-plane domains do not change much as seen in figure 5.7. The change in contrast and brightness of the MFM images is due to increase in the magnetic moment of the MFM tip under external fields. The stripes marked by a cyan arrow in figure 5.7(b) represent tail-to-tail in-plane domains, which becomes clearer under the field. Possible closure domains are identified in the position marked by a pink arrow in figure 5.7(c). Those closure domains do not show any apparent change in response to the external fields.

5.4 Conclusions

We have studied the magnetic structure of the x = 0.32 compound at various temperatures in the absence or presence of external magnetic field by using low temperature MFM. We found that in the magnetic state the magnetic domains with an out-of-plane magnetization form treelike patterns below 88 K. These magnetic patterns remain highly stable below 60 K and start to undergo a gradual change above 60 K. As the temperature goes higher, more rapid changes in the domain patterns occur. At 88 K, almost all the domains have in-plane magnetization, which reflects that the SRT from out-of-plane magnetization to in-plane magnetization is realized. In-plane domain stripes and closure domains were observed at this temperature. Above 88 K, the in-plane domains gradually disappear. Our results show the SRT occurs from around 70 K to 88 K, which is different from what Asaka et al. [30] observed in the same compound by using LTEM. The domain patterns are more complicated than nano-sized ripples reported by them. The difference is due to sample preparation. For the LTEM study, the sample needs to be ground down to 150 nm or less. This grinding process creates a lot of defects and strain in the sample, which inevitably effects the SRT. Furthermore, as the sample becomes thin, the shape anisotropy energy will play a role in magnetization. Our MFM results are consistent with the macroscopic magnetization measurement [34]. We believe our results represent the bulk magnetic properties of the sample. The SRT is due to the two dimensionality of the system. It is associated with the anisotropic magnetic coupling along the c-axis and in the ab plane. The significant change in the first order anisotropy energy with temperature may be due to the large change in the lattice parameters on which the magnetic coupling between t_{2g} spin moments on neighboring Mn ions sensitively depends. The SRT may also be partially related to a collective excitation induced by short-range two-dimensional ferromagnetic fluctuations in the basal plane.

Appendices

Appendix A

Specification of LTSTM

A.1 Tube Scanner

The tube scanner used in the low temperature STM is 1.2 inch long, 0.25 inch in diameter and 20 mil thick. It is made of PZT-5H (EBL#3). Some physical quantities of the tube scanner are theoretically calculated, see below. The experimental values generally should be at most 20 % off the theoretical ones.

At room temperature, lateral displacement:

$$\Delta L = \frac{0.9 d_{31} V L^2}{d_m t} = 73.8 nm/V \tag{A.1}$$

and Z displacement:

$$Z = \frac{d_{31} L}{t} = 15.7 nm/V \tag{A.2}$$

and capacitance of four quadrants:

$$C = \frac{2K^T \varepsilon \pi L}{ln(d_{OD}/d_{ID})} = 33.5 nF \tag{A.3}$$

where $d_m = (d_{OD} + d_{ID})/2$; L is the length of the tube scanner; $d_{31} = -2.75 \mathring{A}/V$ at 300 K; $-0.09 \mathring{A}/V$, at 77 K; $d_{31} = -0.07 \mathring{A}/V$, at 20 K; $-0.05 \mathring{A}/V$, at 4 K; $K^T = 3450$ at 300 K [12]

The tube scanner sensitivity settings in RHK are conveniently set as follows:

- X,Y scan/offset sensitivity: 75nm/V
- Z scan sensitivity: 13nm/V
- The others are not important.

The real sensitivities of the scanner are equal to the nominal sensitivities divided by scale factors shown below.

- At room temperature, $F_{xy} = 0.98 \pm 0.08$ and $F_z = 0.93 \pm 0.06$.
- At 80K (LN_2 cooling),$F_{xy} = 2.8 \pm 0.2$ and $F_z = 2.7 \pm 0.2$.
- At 20K (LHe cooling), around 4.5 for both lateral and z directions. Need to confirm.

Due to temperature changes of the STM head, the tube scanner shows thermal drift. The thermal drift of the tube scanner depends on its working temperatures. Usually the lower the temperature at which the tube scanner works, the smaller the thermal drift that it exhibits. The thermal drift rates at three different temperatures are listed below:

- At room temperature, 15 nm/hour
- At 80K (LN_2 cooling), 5 nm/hour
- At 20K (LHe cooling), 5 Å/hour.

A.2 Dewar

The outer dewar with ~ 8 liters in volume is filled with LN_2 during low temperature experiments. It needs to refill every 24 hours. The inner dewar with ~ 7 liters in volume can be filled with either LN_2 or LHe depending on our needs. When filled with LN_2, it needs to refill every week; When filled with LHe, it needs to refill every 40 hours. The STM can be cooled down to 80 K when both dewars are filled with LN_2, and it can be cooled down to 20 K when the inner dewar is filled with LHe while the outer dewar is filled with LN_2.

A.3 Vacuum in the STM Chamber

In order to increase the thermal conductivity, a layer of indium is inserted in between the colder finger and the bottom of the inner dewar. Because of this, we can not bake the area near the dewars at high temperature. At room temperature, the vacuum in the main chamber can reach 7×10^{-10} torr. After the dewars are cooled down, the vacuum can reach 2×10^{-10} torr or better due to cryogenic pumping.

Appendix B

Tip Etching

B.1 Etching Pt/Ir Tips

We use calcium chloride aqueous solution, with a volume ratio of 50% saturated calcium chloride aqueous solution to 50% distilled water or deionized water (e.g. 24 g $CaCl_2$, 60 ml water), as an electrolyte to etch Pr/Ir tips. The whole etching process is divided into two steps [14]. In the first step, a sharp tip with rough and dirty surface is obtained by applying a high AC voltage (35 V) between the tip and etchant. Generally it takes 10 minutes to get one sharp tip. In the second step, fine polishing is employed to the sharp tip to smooth its surface and remove the impurities. To do so, we place the very end of the tip into a loop of film etchant by using a 60 X long working distance optical microscope. A ~ 2 AC voltage is applied between the loop and tip. It takes about 3 minutes to finish this step.

B.2 Etching Tungsten Tips

Tungsten tips are widely used by STM users around the world. There are numerous ways to prepare a sharp tungsten tip. We use an electronic circuit to control the etching process [76], see figure B.1. Basically, the circuit

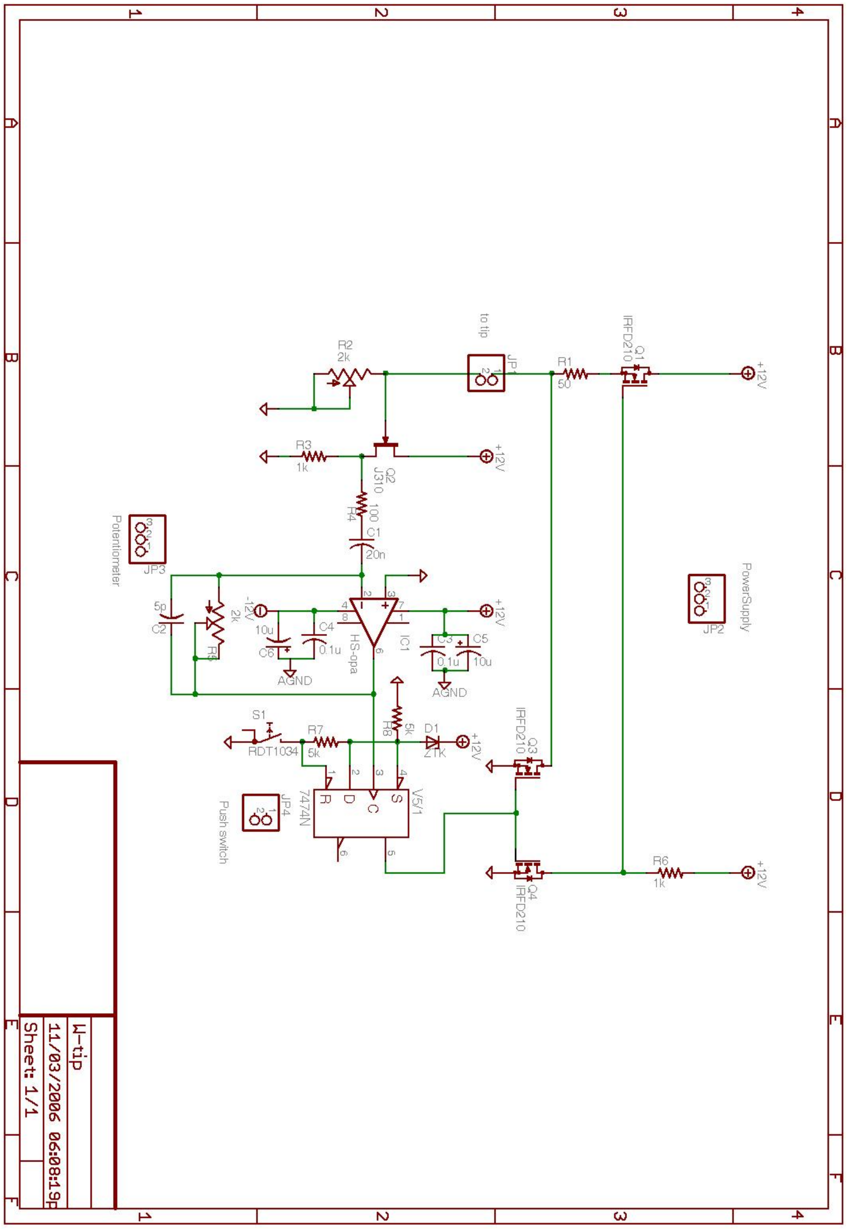

Figure B.1: Schematic of the circuit for etching tungsten tips is used to cut off the etching voltage immediately after the etching is finished. A sharp tip can be easily obtained in this way in 10 minutes.

Appendix C

Lock-in Technique Used in STS

C.1 Introduction

Scanning tunneling spectroscopy (STS) reveals the local density of states (LDOS) of a sample's surface. Because the LDOS carries a lot of information about the physical properties of a sample, it is always desirable to obtain reproducible STS of the sample. Generally, there are two ways to obtain STS. One is to numerically calculate the conductance (dI/dV) from IV curves. The other is to use a lock-in amplifier to directly take dI/dV. In the former way, IV curves are smoothed by using Savitzky-Golay filtering method and then numerically differentiated. In order to increase the signal to noise ratio, a lot of data points in one IV curve are required. In the latter way, a bias modulation signal with frequency f is added and a lock-in amplifier is used to lock the signal with frequency f from the tunneling current. The output of the lock-in amplifier is proportional to dI/dV. Less data points are required in one IV curve in this case.

C.2 Equations

When the bias voltage is modulated, the tunneling current can be expressed as:

$$I(V + \Delta V sin(\omega t)) = I(V) + \frac{dI}{dV}\Delta V sin(\omega t) + ... \qquad \text{(C.1)}$$

$I(V + \Delta V sin(\omega t))$ is expanded in form of the Taylor series. Δ V is very small. So the approximation is made only up to the first order of the Taylor series and the higher orders are neglected.

The lock-in amplifier outputs $\frac{dI}{dV}\Delta V$ through its X channel. The X channel is connected to one of the analog inputs on the RHK controller. Then the $\frac{dI}{dV}\Delta V$ signal is simultaneously recorded along with IV data.

In the tunneling current circuit loop, the tunneling junction is treated as a big resistor (GΩ) in parallel with an equivalent stray capacitor (100pF) mainly due to tunneling current cable and the current amplifier. At f = 600 Hz, the impedance of the stray capacitor is much larger than that of the tunneling junction. This causes some trouble in measuring the conductance of the tunneling junction. Some special care must be taken in order to eliminate the effect of the stray capacitor.

The resultant admittance of the tunneling current circuit loop is:

$$G = \frac{1}{R_{tj}} + j2\pi f C_s. \qquad \text{(C.2)}$$

where $\frac{1}{R_{tj}}$ is the conductance of the tunneling junction, C_s is the total capacitance of the tunneling current loop.

C.3 Lock-in Technique

There are four important parameters in a lock-in amplifier, which are frequency, time constant, phase and sensitivity.

An AC signal with frequency f_d generated by the lock-in amplifier is added to the bias voltage. The frequency f_d should be chosen to be different from any noise frequencies so that a high signal-to-noise ratio can be achieved. f_d should also be smaller than the cut-off frequency of the current amplifier (f_c) (usually $f_d \leq 0.7 f_c$).

The time constant should be set $\tau \leq T_s$, usually $\tau = T_s/3$, where T_s is the sampling time over a bias voltage step. So the noise is averaged out but the peak height and width of the signal are preserved. The time constant τ should also satisfy $\tau \geq \frac{1}{f_d}$ in order to have a high signal-to-noise ratio.

Before using the lock-in amplifier, we should set the phase properly, otherwise we won't be able to obtain the conductance through the X channel. The way to set the phase is the following:

1. Wait until the feedback is stable.
2. Open the feedback loop and withdraw the tip until the tunneling current disappears.
3. Turn on the modulation signal
4. Zero the real part of the output by adjusting the phase in the lock-in amplifier.

5. Turn off the modulation signal.
6. Close the feedback loop.

The sensitivity determines the resolution of the output signal. It should be chosen to maximize the resolution. The conductance of the tunneling junction is given by:

$$\frac{dI}{dV}\Delta V = \frac{V_{out}}{10} \times Sensitivity. \tag{C.3}$$

The following are a set of parameters we tried to take dI/dV.

- the modulation voltage V_{rms}= 10 meV with a frequency of 600-800 Hz
- the time constant τ =10-30 ms
- the pre-sample delay time t_{psd} = 50 ms and sampling time t_s = 30-90 ms
- the spectrum delay time t_{sd} = 100 ms
- the bias voltage sweep rate V_{sweep} = 5 V/s and setup rate V_{setup} = 10 V/s

The equation [1] to estimate the time to finish a pair of IV curves is

$$t = t_{sd}+((t_{psd}+t_s)\times N+\frac{|V_{final}-V_{initial}|}{V_{sweep}})\times 2+\frac{|V_{initial}-V_{setpoint}|}{V_{setup}}+\frac{|V_{final}-V_{setpoint}|}{V_{setup}} \tag{C.4}$$

---

[1] Additional stabilization intervals should be added if more than a pair of IV curves are taken

Bibliography

[1] G. Binnig, H. Rohrer, Ch. Gerber, and E. Weibel. *Phys. Rev. Lett.*, 49:57, 1982.

[2] V. M. Hallmark, S. Chiang, J. F. Rabolt, J. D. Swalen, and R. J. Wilson. *Phys. Rev. Lett.*, 59:2879, 1988.

[3] R. M. Feenstra and J. A. Stroscio. *Physcia Scripta*, T19:55, 1987.

[4] R. J. Hamers. *Ann. Rev. Phys. Chem.*, 40:531, 1989.

[5] S. H. Pan, J. P. O'Neal, R. L. Badzey, C. Chamon, H. Ding, J. R. Engelbrecht, Z. Wang, H. Eisaki, S. Uchida, A. K. Gupta, K.-W. Ng, E. W. Hudson, K. M. Lang, and J. C. Davis. *Nature*, 413:282, 2001.

[6] H. L. Edwards, J. T. Markert, and A. L. de Lozanne. *Phys. Rev. Lett.*, 69:2967, 1992.

[7] M. F. Crommie, C. P. Lutz, and D. M. Eigler. *Science*, 262:218, 1992.

[8] A. J. Heinrich, J. A. Gupta, C. P. Lutz, and D. M. Eigler. *Science*, 306:466, 2004.

[9] J. Bardeen. *Phys. Rev. Lett.*, 6:57, 1960.

[10] J. Tersoff and D. R. Hamann. *Phys. Rev. Lett.*, 50:1998, 1983.

[11] J. Tersoff and D. R. Hamann. *Phys. Rev. B*, 31:805, 1985.

[12] C. Julian Chen. *Introduction to Scanning Tunneling Microscopy.* Oxford University Press, New York, Oxford, 1993.

[13] R. J. Hamers, R. M. Tromp, and J. E. Demuth. *Phys. Rev. Lett.*, 56:1972, 1986.

[14] Allan J. Melmed. *J. Vac. Sci. Technol. B*, 9:601, 1991.

[15] S. Jin, T. H. Tiefel, M. McCormack, R. A. Fastnacht, R. Ramesh, and L. H. Chen. *Science*, 264:413, 1994.

[16] John B. Goodenough. *Localized to Itinerant Electronic Transition in Perovskite Oxides.* Springer-Verlag Berlin Heidelberg, New York, 2001.

[17] H. Y. Hwang, S-W. Cheong, P. G. Radaelli, M. Marezio, , and B. Batlogg. *Phys. Rev. Lett.*, 75:914, 1995.

[18] Y. Tokura and N. Nagaosa. *Science*, 288:462, 2000.

[19] C. Zener. *Phys. Rev.*, 82:403, 1951.

[20] P. W. Anderson and H. Hasegawa. *Phys. Rev.*, 100:675, 1955.

[21] Y. Moritomo, A. Asamitsu, H. Kuwahara, and Y. Tokura. *Nature*, 380:141, 1996.

[22] J. F. Mitchell, D. N. Argyriou, A. Berger, K. E. Gray, R. Osborn, and U. Welp. *J. Phys. Chem.*, 44:10731, 2001.

[23] Masato Kubota, Hirofumi Fujioka, Kazuma Hirota, Kenji Ohoyama, Yutaka Moritomo, Hideki Yoshizawa, and Yasuo Endoh. *J. Phys. Soc. Jpn.*, 69:1601, 2000.

[24] J. S Zhou, J. B. Goodenough, and J. F. Mitchell. *Phys. Rev. B*, 61:R9217, 2000.

[25] D. N. Argyriou, J. F. Mitchell, J. B. Goodenough, O. Chmaissem, S. Short, and J. D. Jorgensen. *Phys. Rev. Lett.*, 78:1568, 1997.

[26] T. Kimura, Y. Tomioka, A. Asamitsu, and Y. Tokura. *Phys. Rev. Lett.*, 81:5920, 1998.

[27] J. F. Mitchell, D. N. Argyriou, J. D. Jorgensen, D. G. Hinks, C. D. Potter, and S. D. Bader. *Phys. Rev. B*, 55:63, 1997.

[28] J. S Zhou, J. B. Goodenough, and J. F. Mitchell. *Phys. Rev. B*, 58:R579, 1998.

[29] N. Mannella, W. L. Yang, X. J. Zhou, H. Zheng, J. F. Mitchell, J. Zaanen, T. P. Devereaux, N. Nagaosa, Z. Hussain, and Z.-X. Shen. *Nature*, 438:474, 2005.

[30] T. Asaka, T. Kimura, T. Nagai, X. Z. Yu, K. Kimoto, Y. Tokura, and Y. Matsui. *Phys. Rev. Lett.*, 95:227204, 2005.

[31] T. Kimura and Y. Tokura. *Annu. Rev. Mater. Sci.*, 30:451, 2000.

[32] J. B. Goodenough. *Phys. Rev.*, 100:564, 1955.

[33] K. H. J. Buschow and F. R. de Boer. *Physics of Magnetism and Magnetic Materials.* Kluwer Academic Plenum Publishers, New York, 2003.

[34] U. Welp, A. Berger, V. K. Vlasko-Vlasov, QingAn Li, K. E. Gray, and J. F. Mitchell. *Phys. Rev. B*, 89:621, 2000.

[35] W. Archibald, J. S. Zhou, and J. B. Goodenough. *Phys. Rev. B*, 53:14445, 1996.

[36] J. B. Goodenough. *J. Appl. Phys.*, 81:5330, 1997.

[37] P. Schiffer, A. P. Ramirez, W. Bao, and S-W. Cheong. *Phys. Rev. Lett.*, 75:3336, 1995.

[38] T. Okuda, A. Asamitsu, Y. Tomioka, T. Kimura, Y. Taguchi, and Y. Tokura. *Phys. Rev. Lett.*, 81:3203, 1998.

[39] A. J. Millis, P. B. Littlewood, and B. I. Shraiman. *Phys. Rev. Lett.*, 74:5144, 1995.

[40] T. V. Ramakrsihnan, H. R. Krishnamurthy, S. R. Hassan, and G. Venketeswara Pai. *Phys. Rev. Lett.*, 92:157203, 2004.

[41] E. W. Hudson, S. H. Pan, A. K. Gupta, K.-W. Ng, and J. C. Davis. *Science*, 285:88, 1999.

[42] R. Matzdorf, Z. Fang, Ismail, Jiandi Zhang, T. Kimura, Y. Tokura, K. Terakura, and E. W. Plummer. *Science*, 289:746, 2000.

[43] Jeehoon Kim, Junwei Huang, J. S. Zhou, J. B. Goodenough, and Alex de Lozanne. *Submitted to PRL.*

[44] T. Okuda, T. Kimura, and Y. Tokura. *Phys. Rev. B*, 60:3370, 1999.

[45] F. Loviat, H. M. Ronnow, Ch Renner, G. Aeppli, T. Kimura, and Y. Tokura. *Nanotechnology*, 18:044020, 2007.

[46] J. X. Ma, D. T. Gillaspie, E. W. Plummer, and J. Shen. *Phys. Rev. Lett.*, 95:237210, 2005.

[47] K. Schulte, M. A. James, L. H. Tjeng, P. G. Steeneken, G. A. Sawatzky, R. Suryanarayanan, G. Dhalenne, and A. Revcolevschi. *Phys. Rev. B*, 64:134428, 2001.

[48] D.S. Dessau, T. Saitoh, C. H. Park, Z. X. Shen, P. Villella, N. Hamada, Y. Moritomo, and Y. Tokura. *Phys. Rev. Lett.*, 81:192, 1998.

[49] T. Saitoh, D. S. Dessau, Y. Moritomo, T. Kimura, Y. Tokura, and N. Hamada. *Phys. Rev. B*, 62:1039, 2000.

[50] Y. D. Chuang, A. D. Gromko, D. S. Dessau, T. Kimura, and Y. Tokura. *Science*, 292:1509, 2001.

[51] H. M. Ronnow, Ch. Renner, G. Aeppli, T. Kimura, and Y. Tokura. *Nature*, 440:1025, 2006.

[52] P.W. Anderson and N.P. Ong. *J Phys. Chem. Solid*, 67:1, 2006.

[53] J.-H. Park, T. Kimura, and Y. Tokura. *Phys. Rev. B*, 58:R13330, 1998.

[54] J. W. Freeland, K. E. Gray, L. Ozyuzer, P. Berghuis, Elvira Badica, J. Kavich, H. Zheng, and J. F. Mitchell. *Nature Materials*, 4:62, 2005.

[55] M. Konoto, T. Kohashi, K. Koike, T. Arima, Y. Kaneko, T. Kimura, and Y. Tokura. *Phys. Rev. B*, 71:184441, 2005.

[56] X. Y. Huang, O. N. Mryasov, D. L. Novikov, and A. J. Freeman. *Phys. Rev. B*, 62:13318, 2000.

[57] B. J. Campbell, R. Osborn, D. N. Argyriou, L. Vasiliu-Doloc, J. F. Mitchell, S. K. Sinha3, U. Ruett, C. D. Ling, Z. Islam, and J. W. Lynn. *Phys. Rev. B*, 65:014427, 2001.

[58] L. Vasiliu-Doloc, S. Rosenkranz, R. Osborn, S. K. Sinha, J. W. Lynn, J. Mesot, O. H. Seeck, G. Preosti, A. J. Fedro, and J. F. Mitchell. *Phys. Rev. Lett.*, 83:4393, 1999.

[59] T. Cren, D. Roditchev, W. Sacks, and J. Klein. *Europhys. Lett.*, 54:84, 2001.

[60] D. N. Argyriou, J. W. Lynn, R. Osborn, B. Campbell, J. F. Mitchell, U. Ruett, H. N. Bordallo, A. Wildes, and C. D. Ling. *Phys. Rev. Lett.*, 89:036401, 2002.

[61] Akihisa Koizumi, Toshihiro Nagao, Nobuhiko Sakai, Kazuma Hirota, and Yoich Murakami. *Phys. Rev. B*, 74:012408, 2006.

[62] Tomohiro Shibata, Bruce Bunker, J.F. Mitchell, and Peter Schiffer. *Phys. Rev. Lett.*, 74:012408, 2006.

[63] R. Wiesendanger, H.-J. Gntherodt, G. Gntherodt, R. J. Gambino, and R. Ruf. *Phys. Rev. Lett.*, 65:247, 1990.

[64] A. Hubert and R. Schafer. *Magnetic Domains: The analysis of Magnetic Microstructures.* Springer-Verlag, Berlin, Germany, 1998.

[65] M. Uehara, S. Mori, C. H. Chen, and S.-W. Cheong. *Nature*, 399:560, 1999.

[66] Qingyou Lu, Chun-Che Chen, and Alex de Lozanne. *Science*, 276:2006, 1997.

[67] Liuwan Zhang, Casey Israel, Amlan Biswas, R. L. Greene, and Alex de Lozanne. *Science*, 298:805, 2002.

[68] G. Binnig, H. Rohrer, Ch. Gerber, and E. Weibel. *Phys. Rev. Lett.*, 56:930, 1986.

[69] Tien-Ming Chuang and Alex de Lozanne. *Rev. Sci. Instrum.*, 78:053710, 2007.

[70] Casey Israel, Changbae Hyun, Alex de Lozanne, Soohyon Phark, and Z. G. Khim. *Rev. Sci. Instrum.*, 77:023704, 2006.

[71] U. Dürig. *Appl. Phys. Lett.*, 75:433, 1999.

[72] J. Unguris, M. R., Scheinfein, R. J. Celotta, and D. T. Pierce. *Appl. Phys. Lett.*, 55:2553, 1989.

[73] H. J Williams, F. G Foster, and E. A Wood. *Phys. Rev.*, 82:119, 1951.

[74] J. B. Goodenough. *Phys. Rev.*, 102:356, 1956.

[75] B. D. Cullity. *Introduction to Magnetic Materials.* Addison-Wesley Publishing Company, Reading, Massachusetts, 1972.

[76] Yoshiaki Nakamura, Yutaka Mera, and Koji Maedaa. *Rev. Sci. Instrum.*, 70:3373, 1999.

[77] T. Hanaguri, C. Lupien, Y. Kohsaka, D-H. Lee, M. Azuma, M. Takano, H. Takagi, and J. C. Davis. *Nature*, 430:1001, 2004.

Vita

Junwei Huang was born in Jintian, a small village in Shengxian, Zhejiang, China, on November 9, 1975, the son of Maoliang Huang and Yazhen Ying. He graduated from Nanjing University, Nanjing, China, in July 1998 with a Bachelor's degree in physics. Two months later, he went to the Department of Physics of Peking University, Beijing, China to begin his graduate career. Under his advisor Prof. Shousheng Yan, he carried out a systematic study on electrical thermopower of the superconductor magnesium diboride. In July 2001, he received a Master's degree in physics. From there, he entered the Department of Physics of the University of Texas at Austin and began to work in Dr. Alex de Lozanne's Scanning Probe Microscopy lab. His Ph.D. work focused on low temperature scanning tunneling microscopy and magnetic force microscopy investigation of layered manganites.

Permanent address: 1704 Nelms Dr. Apt. 1537
Austin, Texas 78744

This dissertation was typeset with LaTeX[†] by the author.

[†] LaTeX is a document preparation system developed by Leslie Lamport as a special version of Donald Knuth's TeX Program.